CASL-U-2018-1676-000

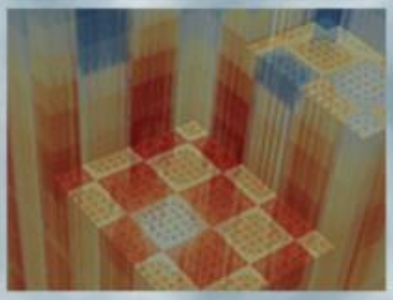

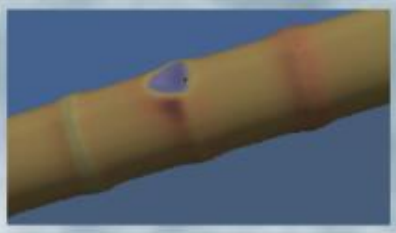

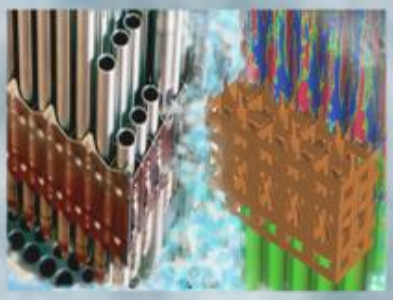

Predicting Departure from Nucleate Boiling with Advanced Data- and Physics-Driven Approaches

Milestone: L4:PHI.CTF.P17.01

Xingang Zhao

Massachusetts Institute of Technology

10/12/2018

REVISION LOG

Revision	Date	Affected Pages	Revision Description
0	10/12/2018	All	Initial Release

Document pages that are:

Export Controlled ____none_____

IP/Proprietary/NDA Controlled ____none_____

Sensitive Controlled ____none_____

Requested Distribution:

To:

Copy:

EXECUTIVE SUMMARY

The subcooled and low-quality saturated flow boiling critical heat flux (CHF) corresponding to the departure from nucleate boiling (DNB) is one of the major limiting factors in the design and operation of pressurized water reactors (PWRs). Due to lack of agreement on its physical mechanisms, development of an accurate DNB-type CHF model has been elusive. The various steady-state (SS) predictive tools that have been proposed can be grouped into two categories: (1) data-driven methods—namely best-fit empirical correlations and look-up tables that result in relatively good agreement with specific experimental datasets but often fail to extend beyond their ranges of validity, and (2) the physics-based mechanistic models that rely on reasonable yet limited understanding of the underlying physics and apply constitutive relations to close the conservation equations.

On one hand, with recent advances in computational capabilities and optimization techniques, machine learning (ML)-based methods constitute an alternative and a more advanced, data-driven approach. With enough data, they can be particularly useful in engineering fields where the physical phenomena are complex and challenging to model. On the other hand, a state-of-the-art physics-driven approach would not only provide more accurate prediction of SS CHF, but it would also help better understand and model transient applications.

The data-driven regression models use deep feed-forward neural networks (NNs) and random forests to cross-validate with 1,865 CHF test cases, covering a wide range of flow conditions and channel geometries. The best-estimate ML-based predictors compare favorably with the widely used look-up table for annulus and plate, and sensitivity analysis has confirmed their effectiveness. The key advantage of ML-based methods is their online extensibility of applicability domain. The proposed physics-driven approach combines key assumptions and parameters in the relatively well-accepted theories of liquid sublayer dryout and near-wall bubble crowding. A more realistic understanding of local mechanisms has been modeled. The new model has been optimized and validated against 1,439 tube data, and it shows considerably improved performance when compared to a recent mechanistic model, demonstrating unbiased close agreement with measurements over a wide range of operating conditions.

Future work will extend the improved physics-driven model to non-tube geometry applications and will couple the model with ML via a hybrid approach. The mechanistic SS work will also serve to improve understanding and to model transient CHF scenarios.

(This page intentionally left blank)

CONTENTS

EXECUTIVE SUMMARY iii

CONTENTS v

FIGURES vi

TABLES vii

NOMENCLATURE viii

1. INTRODUCTION 1
   1.1. Background and Motivation 1
   1.2. Work Scope 1

2. ADVANCED DATA-DRIVEN APPROACH: ML-BASED METHODS 2
   2.1. Overview 2
   2.2. Data Description 3
   2.3. Training, Validation, and Comparison 3
   2.4. Sensitivity Analysis 9

3. ADVANCED PHYSICS-DRIVEN APPROACH: MECHANISTIC MODEL 9
   3.1. Overview 9
   3.2. New Model Description 12
   3.3. Model Evaluation 18

4. CONCLUSIONS AND FUTURE WORK 34

ACKNOWLEDGMENTS 35

REFERENCES 36

FIGURES

Figure 1. Example of a 3/5/6/2 NN architecture. 2
Figure 2. Simplified RF algorithm structure. 2
Figure 3. Cumulative data fraction of absolute relative error for best-estimate ML-based predictors and look-up table. 6
Figure 4. Predicted vs. measured CHF with best-estimate ML-based predictors and look-up table. 8
Figure 5. Simplified sketch of the liquid sublayer dryout theory. 10
Figure 6. Schematic view of a stable vapor blanket in the Liu model.[21] 11
Figure 7. Schematic view of the flow channel in a round tube at near-CHF conditions. 13
Figure 8. Predicted vs. measured tube CHF with look-up table, Liu model, best-estimate NN (10-fold), and new model. 21
Figure 9. Tube CHF relative error vs. pressure. 23
Figure 10. Tube CHF relative error vs. mass flux. 26
Figure 11. Tube CHF relative error vs. exit equilibrium quality. 28
Figure 12. Tube CHF relative error vs. tube diameter. 31
Figure 13. Tube CHF relative error vs. length-to-diameter ratio. 33

TABLES

Table 1. CHF dataset: baseline input variable ranges for ML-based methods. 3
Table 2. ML-based CHF predictor performance on all data: sensitivity study. 9
Table 3. Optimized piecewise constant function for c_3 in Eq. (9). 15
Table 4. Predicted tube SS CHF performance with different models. 18

NOMENCLATURE

A: area
C_D: drag coefficient
C_p: specific heat at constant pressure
D: diameter
F: force
f: friction factor
G: mass flux
g: gravitational acceleration
h_{fg}: latent heat of vaporization
L: length
$\dot{m}$: mass flow rate
P: pressure
q'': heat flux
Re: Reynolds number
T: temperature
U: velocity
U_τ: friction velocity
x: flow quality
x_e: equilibrium quality
y: distance from the wall [to bubble centerline]
y^+: non-dimensional distance from the wall

Greek symbols

α: void fraction
δ: liquid sublayer thickness
δ_b: bubble region thickness
ε: surface roughness
η: fraction of cross-sectional area
λ: critical wavelength
ρ: density
σ: surface tension
τ: shear stress
μ: dynamic viscosity

Subscripts

1: interface I
2: interface II / local region on the right-hand side of interface II
b: bubble region (bubbly layer)
B: vapor blanket
c: core region
d: departure
f: saturated liquid
g: saturated vapor
l: liquid
out: channel outlet
sat: saturation
v: vapor
w: wall

Acronyms

API: application programming interface
BWR: boiling water reactor
CHF: critical heat flux
DNB: departure from nucleate boiling
ML: machine learning
NN: neural network
PWR: pressurized water reactor
ReLU: rectified linear unit
RF: random forest
RIA: reactivity-initiated accident
rRMSE: root mean squared relative error
SS: steady state
V&V: validation and verification

(This page intentionally left blank)

1. INTRODUCTION

1.1. Background and Motivation

The departure from nucleate boiling (DNB) crisis can trigger a set of cascading failures in a pressurized water reactor (PWR). Due to a lack of agreement in the physical mechanisms, developing an accurate model for DNB-type critical heat flux (CHF) has been elusive. During the past few decades, the reactor thermal-hydraulics community has proposed over 500 predictive tools under steady-state (SS) conditions. The data-driven methods—namely best-fit empirical correlations and look-up tables—result in relatively good agreement with specific experimental datasets, but they often fail to extend beyond their ranges of validity. The physics-based mechanistic models rely on a reasonable yet limited understanding of the underlying physics supplemented with mostly empirical closure relations.

Modeling and simulation of PWR transients in system or subchannel codes are currently performed with a quasi–steady-state approach in which SS correlations or look-up tables are applied with time-dependent flow variables. However, existing experimental studies[1] have revealed that during fast transients such as a reactivity-initiated accident (RIA), the CHF values can become significantly higher than those in SS or slow transient scenarios; such an approach would lead to overly conservative DNB predictions.

A robust, mechanistic transient CHF model was recently proposed.[1] It clearly outperformed the quasi–steady-state approach, and it generally agreed well with measurements from three sets of power transient experiments with different channel geometries at different operating conditions. However, a basic assumption in the model was made such that the corresponding initial value (i.e., SS CHF which serves as the starting point in the transient model) was estimated to be the measured CHF at the slowest power ramp rate for each test case. This was done because the widely used look-up table method could not be used to perform proper validation and verification (V&V) without correction factor tuning for geometries other than round tubes.[1,2] Moreover, the model still significantly under-estimated CHF for very fast transients at low pressures, and the assumed DNB triggering mechanisms would require further investigation.

On one hand, with recent advances in computational capabilities and optimization techniques, machine learning (ML) methods constitute a more advanced, alternative, data-driven approach. With enough data, ML methods can be particularly useful when physical phenomena are complex and challenging to model. On the other hand, a state-of-the-art, physics-driven approach would not only provide more robust, accurate prediction of SS CHF but also help better understand and model the mechanisms during transients so as to further improve the predictive capabilities of the transient CHF model.

1.2. Work Scope

This report will first present work related to ML-based SS CHF predictors in subcooled and low-quality saturated flow boiling. Two advanced regression methods were applied: deep feed-forward neural network (NN), and tree-based random forest (RF). A dataset covering a wide range of flow conditions and channel geometries was collected for model training and validation, and results were compared with the prevalent 2006 CHF look-up table.[3] In the second place, an advanced mechanistic model combining the two most generally accepted DNB theories—liquid sublayer dryout and near-wall bubble crowding—will be proposed and evaluated against round tube data as well as other predictive tools.

2. ADVANCED DATA-DRIVEN APPROACH: ML-BASED METHODS

2.1. Overview

As illustrated in Figure 1, the deep feed-forward NN is a collection of multilayer, fully-connected units ("neurons"), capable of non-linear mapping via activation functions (also known as transfer functions). The weights of the units are updated by the backward propagation learning algorithm using gradient descent. The random forest is a fast, flexible, tree-based ML method that produces reliable results without much tuning of hyperparameters.[a] By randomly selecting observations and features using the bootstrap aggregation ("bagging")[b] technique, multiple decision trees are built and predictions are then averaged, as depicted in Figure 2. Both of these regression methods allow for high generalization ability when properly sampled and trained, and the *black-box* characteristics of ML-based predictors make them powerful, precluding the need for explicit mathematical modeling.

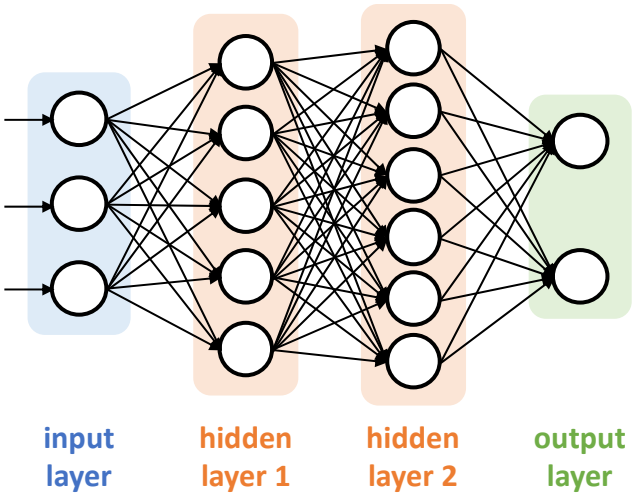

Figure 1. Example of a 3/5/6/2 NN architecture.

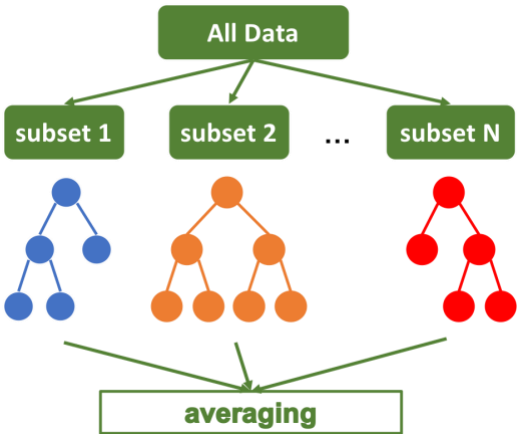

Figure 2. Simplified RF algorithm structure.

[a] *Hyperparameters* are parameters with values that are set before learning starts.
[b] *Bagging* is a special case of the model averaging approach that is designed to improve accuracy and reduce variance.

Although ML is not new to nuclear engineering, little work has been performed in this area for fluid flow and heat transfer problems. One major obstacle is the lack of experimental data. In regard to SS CHF, most nonproprietary measurements were conducted with steam-water mixtures in internally heated round tubes. None of the recent publications in this field distinguishes DNB with dryout, which is the boiling crisis in a boiling water reactor (BWR).[4–7] Note that DNB only occurs in subcooled and low-quality saturated flow, whereas dryout is triggered at much higher quality and lower heat flux; the term *CHF* is sometimes confusingly used for both boiling crises, though. No recent publications used cross-validation to evaluate their predictors, and none assessed the sensitivity of different hyperparameters or discussed regularization (an ML technique that prevents overfitting and reduces test error).

2.2. Data Description

Relevant publications which include tabulated, nonproprietary, experimental CHF data have been reviewed, and a dataset of 1,865 test cases was collected. The dataset covers a wide range of flow conditions while limiting the focus to DNB-specific characteristics: local equilibrium quality cannot exceed 0.2. The heater geometry was limited to a round tube, an annulus, or one side of a heated plate. Input features collected from raw data comprised exit pressure, mass flux, local (exit) equilibrium quality, equivalent and heated diameter, and heated length. The target/output was CHF and the axial heating profile was uniform. The experimental ranges of the dataset are summarized in Table 1. The SS DNB measurement uncertainties were on the order of 10–15%.[2,16]

While the RF predictor generally performs well with raw inputs, NNs require feature engineering. This process involves transforming measured data into a set of features with properties that can be handled effectively by ML algorithms. For this work, standardization was applied to the input vectors of pressure, mass flux, equivalent and heated diameter, and heated length. The geometry indicator was not included in the baseline input feature vector, and the effectiveness of the predictors will be evaluated later.

Table 1. CHF dataset: baseline input variable ranges for ML-based methods.

Author	Geometry	Feature #1 *pressure* (MPa)	Feature #2 *mass flux* (kg/m^2-s)	Feature #3 *equilibrium quality* (-)	Feature #4 *equivalent diameter* (mm)	Feature #5 *heated diameter* (mm)	Feature #6 *heated length* (mm)	# of data
Inasaka[8]	tube	0.31 to 0.91	4,300 to 6,700	-0.15 to -0.04	3.0	3.0	100	7
Peskov[9]		12 to 20	750 to 5,361	-0.23 to 0.13	10.0	10.0	400 to 1,650	17
Thompson[10]		0.1 to 20.7	542 to 7,975	-0.45 to 0.21	1.0 to 37.5	1.0 to 37.5	25 to 3,048	1,202
Weatherhead[11]		13.8	332 to 2,712	-0.49 to 0.19	7.7 to 11.1	7.7 to 11.1	457	162
Williams[12]		5.5 to 15.2	670 to 4,684	-0.03 to 0.17	9.5	9.5	1,836	51
Beus[13]	annulus	5.5 to 15.5	671 to 3,721	-0.31 to 0.20	5.6	15.2	2,134	77
Janssen[14]		4.1 to 9.7	381 to 5,913	-0.13 to 0.20	4.6 to 22.2	11.3 to 96.3	737 to 2,743	282
Mortimore[15]		8.3 to 13.8	677 to 3,637	-0.13 to 0.20	5.0	13.3	2,134	19
Kossolapov[2]	plate	0.1	0 to 2,078	-0.14 to -0.02	15.0	120.0	10	12
Richenderfer[16]		0.1 to 1.0	1,000 to 2,000	-0.04 to -0.01	15.0	120.0	10	36

2.3. Training, Validation, and Comparison

Both NN and RF predictors were trained and validated using the Keras application programming interface (API) with TensorFlow backend and scikit-learn library in Python 3.6. Given the relatively small

size of the dataset, the shuffled 10-fold cross-validation technique[a] was used to evaluate how the predictors perform on independent validation data. The loss function is the mean squared error, and the performance metric is the root mean squared relative error (rRMSE). The NN weights were initiated from a randomly uniform distribution. Based on the preliminary sensitivity study,[17] the Adam[b] optimization algorithm was applied to update weights and biases; the rectified linear unit (ReLU)[c] activation function was used on the hidden layers due to its high reliability.

The effects of different hyper-parameters were evaluated,[17] including regularization or early stopping, the number of hidden layers and hidden units for NN, the number of epochs[d] for NN, the number of decision trees for RF, and the maximum feature percentage for RF. The best-estimate ML-based CHF predictors were determined for both methods:

- ***NN***: 6/50/50/50/1 architecture (i.e., the input layer has 6 neurons, each of the 3 hidden layers has 50 neurons, and the output layer has 1 neuron), no regularization
- ***RF***: 100 trees, 60% features allowed in individual trees, no early-stopping

As discussed by Zhao,[17] given the dimension of the feature vector and the number of data points, there should not be a concern about over-fitting. The best-estimate predictors are compared against measurements and the well-used 2006 look-up table.[3] The look-up table is a normalized steam-water CHF map for vertical 8 mm tubes that predicts DNB and dryout (not distinguished) as a function of pressure, mass flux, and local equilibrium quality. It was derived from a large data bank covering a wide range of flow conditions. Empirical correction factors were introduced to account for the effects of diameter and other geometry types. The table method is simple to use and has a very low computational cost. Compared to physics-based mechanistic models, it requires no assumptions and closures, although it captures less physical information, and the applicability outside its validity range is doubtful.

Figure 3 and Figure 4 compare the performance of different predictors on all 1,865 data points, to include 1,439 for the tube, 378 for the annulus, and 48 for the one-side heated plate. While the training errors are very small (rRMSE = 7.2% with NN; 5.2% with RF), there is more interest in the cross-validation errors since the goal of ML algorithms is to perform well on unseen future data. The error differences between the approach to train and validate with all data and then analyze for each geometry (shown as "from all data") and the approach to train and validate each geometry separately (shown as "tube/annulus/plate data only") are small, with one exception: NN for plate. This result suggests that the predictions seem to be contained within a reasonable bound. Cross-validation (10-fold) using NN or RF (1) performs in a manner similar to the look-up table for the tube (the look-up table slightly outperforms, but the tube data used in this work was part of the data source for generating the 2006 look-up table) (2) yields reduced errors for the annulus, (3) and significantly outperforms the table method for the plate.

As can be seen in Figures 3(d)–4(d), the two ML-based predictors, which were cross-validated using the entire database, agree closely with each other and with plate measurements. About 90% of predicted data fall within ±20% uncertainty. However, the look-up table tends to dramatically underestimate the one-side heated plate CHF. This underestimation is consistent with previous assessments,[1,2,16] possibly due to the much smaller heated length of the plate heaters used for this work than those of the tubes used for generating the look-up table. It should be noted that if the plate data were not included in training, then similar poor performance would be expected with NN or RF. The key advantage of ML-based predictors is their online extensibility of applicability domain.

[a] randomly shuffled dataset prior to cross-validation, then ten times of "90% train data + 10% validation data" at each time
[b] The Adam optimization algorithm combines the advantages of various extensions of the classic stochastic gradient descent procedure. It is popular in the field of deep learning and requires minimal tuning.
[c] $ReLU(x) = max(0, x)$ is a good approximator, as any function can be approximated with combinations of ReLU.
[d] Each epoch represents one forward pass and one backward pass of all the training examples.

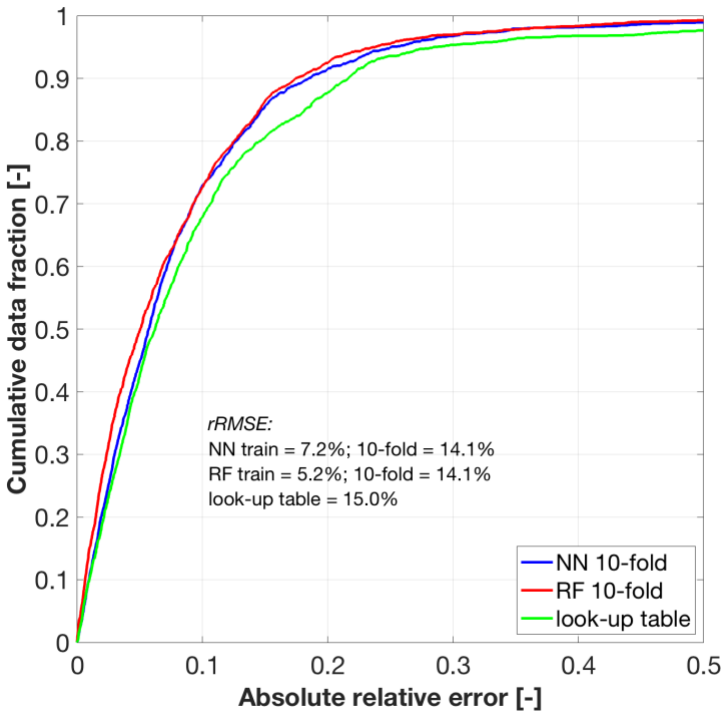

(a) all data

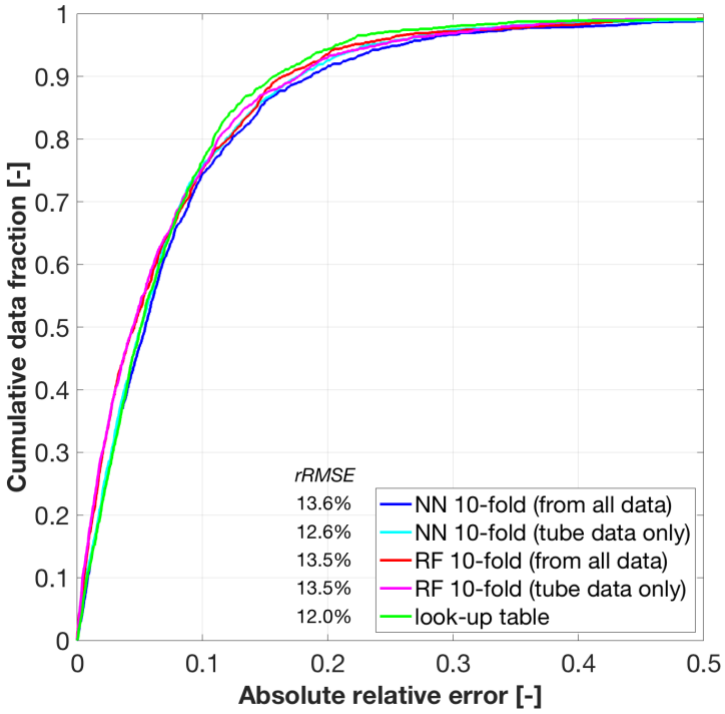

(b) tube data

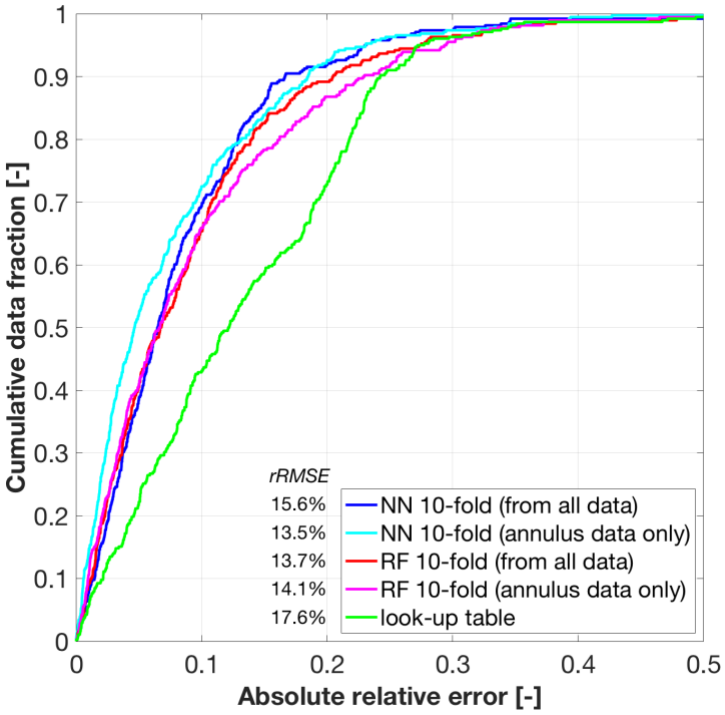

(c) annulus data

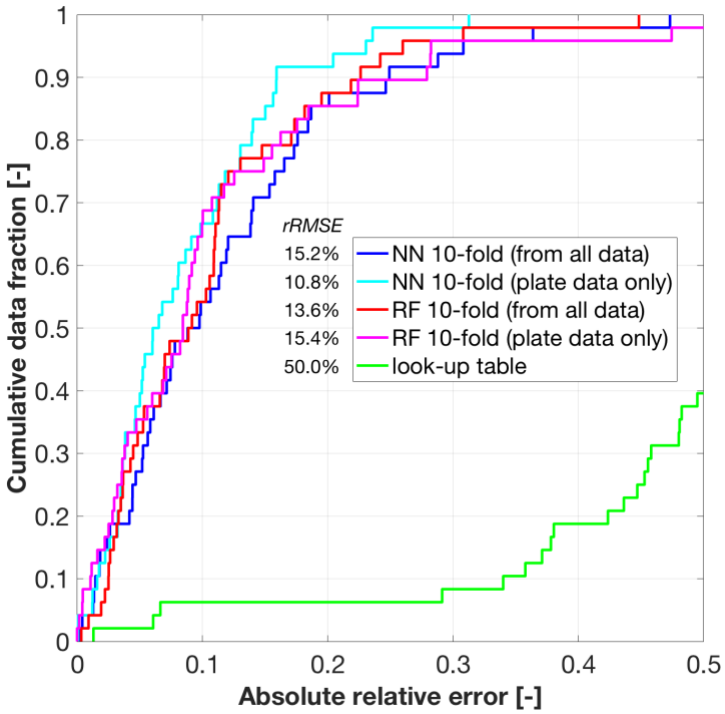

(d) plate data

Figure 3. Cumulative data fraction of absolute relative error for best-estimate ML-based predictors and look-up table.

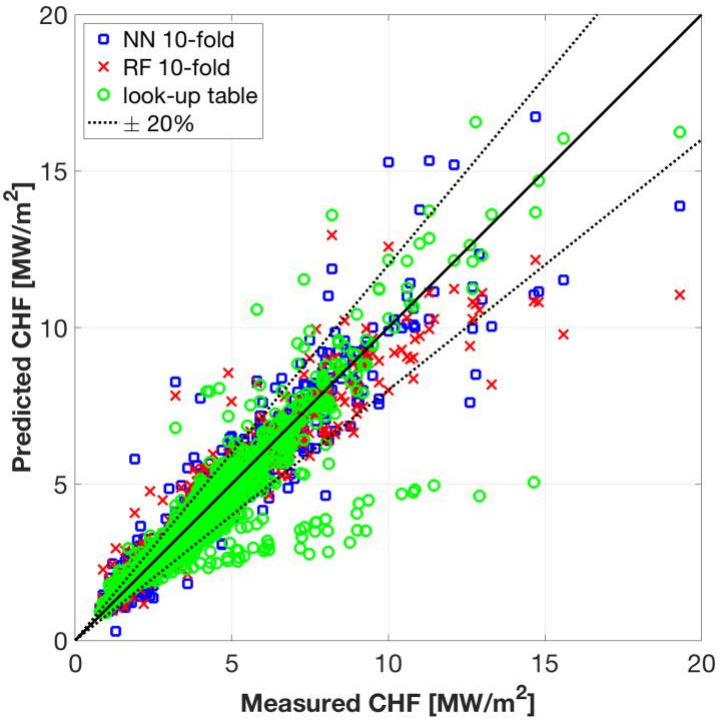

(a) all data

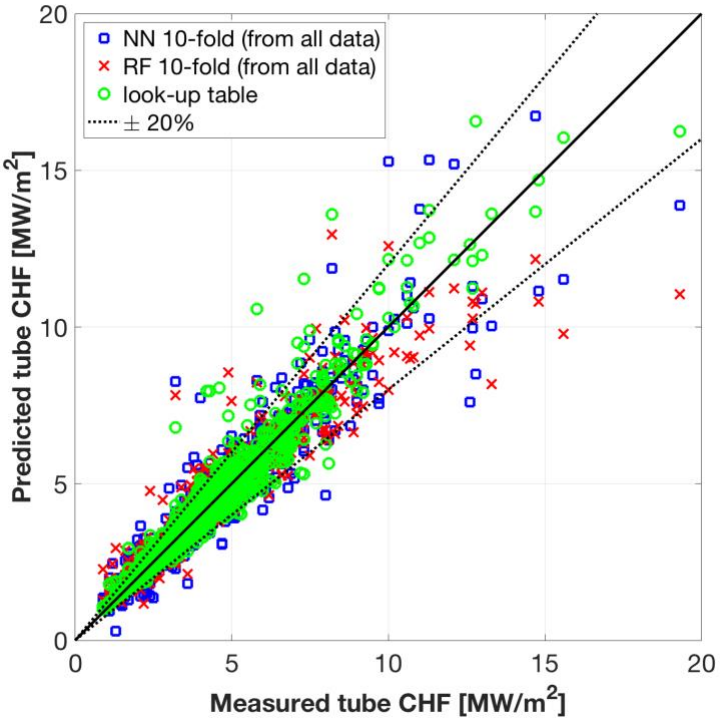

(b) tube data

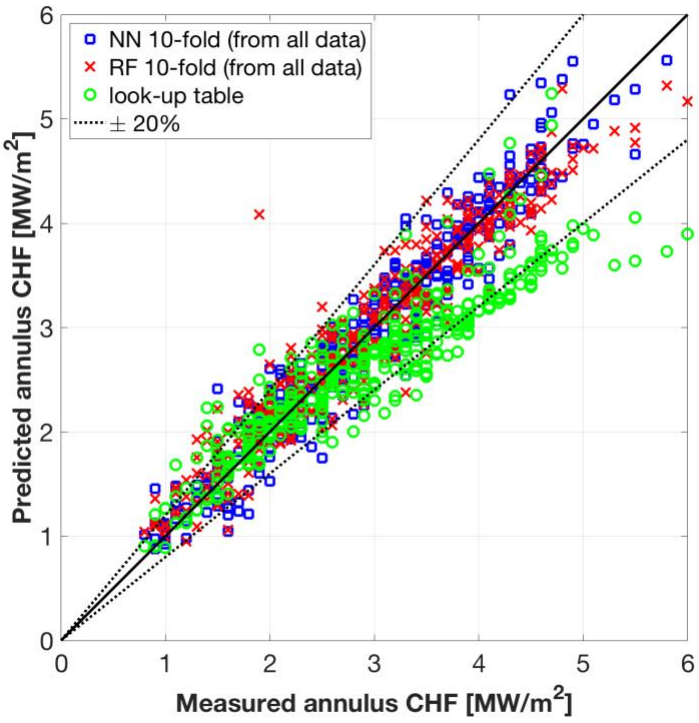

(c) annulus data

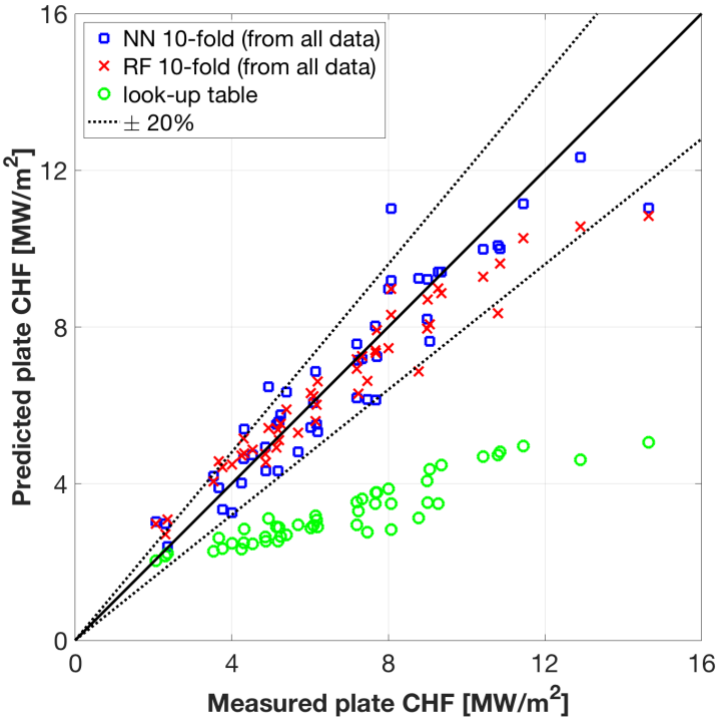

(d) plate data

Figure 4. Predicted vs. measured CHF with best-estimate ML-based predictors and look-up table.

2.4. Sensitivity Analysis

Three sets of sensitivity studies have been conducted to assess the generalizability and effectiveness of the best-estimate ML-based predictors:

i) cross-validation technique: 10-fold vs. 5-fold[a]

ii) input features: with geometry indicator vs. without geometry indicator[b]

iii) choice of input feature #3 (in **Error! Reference source not found.**): local/exit equilibrium quality[c] vs. inlet temperature subcooling

Table 2 summarizes the performance of four scenarios (baseline and three sensitivity cases) on the entire database. The effect of the subsample number in cross-validation (10- vs. 5-fold) is negligible; the ML community highly recommends allocating at least 70% of the available data for training,[d] particularly for small datasets. Adding the geometry indicator increases the input feature dimension, but it also requires more training data to achieve better fitting and to further improve the performance. Replacing the exit equilibrium quality with inlet subcooling clearly reduces the overall error, which is more notable with NN, although the two variables are mathematically inter-derivable using fluid properties and heat balance.

Table 2. ML-based CHF predictor performance on all data: sensitivity study.

Case #	Cross-validation	Geometry indicator	Input feature #3	NN validation rRMSE	NN validation within 20% absolute error	RF validation rRMSE	RF validation within 20% absolute error
baseline	10-fold	no	local quality	0.14	92%	0.14	92%
i	5-fold	no	local quality	0.14	91%	0.14	91%
ii	10-fold	yes	local quality	0.14	92%	0.14	92%
iii	10-fold	no	inlet subcooling	0.09	97%	0.12	94%

3. ADVANCED PHYSICS-DRIVEN APPROACH: MECHANISTIC MODEL

3.1. Overview

Over the years, numerous mechanistic DNB models in flow boiling have been developed, and their approaches can be grouped into six theory categories[18] according to their main respective triggering mechanisms and the following chronological order:

(1) *Liquid layer superheat limit theory* (1965), which assumed that CHF occurs when the liquid layer adjacent to the heated wall reaches its critical enthalpy;

(2) *Boundary layer separation theory* (1968–1975), in which the stagnant liquid underneath the boundary layer evaporates and results in a vapor blanket on the heated wall;

(3) *Liquid flow blockage theory* (1980–1981), which postulated that CHF is triggered when the supply liquid normal to the wall is blocked by the flow of vapor;

[a] five times of "80% train data + 20% validation data" at each time
[b] represented in the form of one-hot encoding (i.e., tube = [1,0,0], annulus = [0,1,0], plate = [0,0,1])
[c] Local quality was favored over inlet subcooling in the baseline input features to be consistent with the look-up table, which is a tabulated function of pressure, mass flux, and local equilibrium quality.
[d] which implies that in n-fold cross-validation, $n \geq 4$

(4) *Vapor removal limit and bubble crowding theory* (1981–1985), which considered a critical value of void fraction in the near wall bubble layer, thus preventing access of supply liquid;

(5) *Liquid sublayer dryout theory* (1988–2010), in which the onset of CHF is caused by the depletion of a thin superheated liquid layer underneath a vapor slug flowing over the heated wall due to evaporation (sketched in Figure 5);

(6) *Interfacial lift-off theory* (1993), in which CHF is assumed to occur when vapor effusion lifts the first wetting front off of the heater's surface (only applicable at high heat fluxes in which bubbles coalesce into a continuous wavy vapor layer).

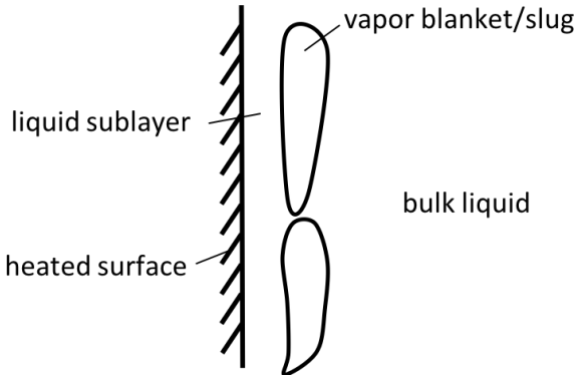

Figure 5. Simplified sketch of the liquid sublayer dryout theory.

Of the six categories, two have received considerable attention: liquid sublayer dryout and near-wall bubble crowding. The former theory has been supported by most of the recent experimental evidence.[18,19] Moreover, it is widely admitted that DNB in subcooled or low-quality saturated flow boiling has strong behavior similarities to pool boiling DNB, both being governed by the hydrodynamic instability of the liquid-vapor interface. It is therefore worth reviewing the state of art on the theory of liquid sublayer dryout proposed by various authors and attempting a more advanced, more realistic physics-driven approach combining the key characteristics of both theories.

In the category of liquid sublayer dryout theory, the original model for subcooled flow boiling in a round tube was proposed by Lee and Mudawar (1988),[20] assuming that a thin vertical distorted cylindrical vapor blanket is formed at near-CHF conditions as a consequence of small bubbles piling up along the near-wall region. The equivalent diameter (or thickness) of the vapor blanket is approximately equal to the bubble departure diameter, whereas its length is assumed to be equal to the critical wavelength of Helmholtz instability at the sublayer-blanket interface. CHF is postulated to occur when the rate of liquid sublayer evaporation exceeds that of the liquid supply from the bulk region. A force balance on the vapor blanket in the radial direction was applied to calculate the liquid sublayer thickness, and three empirical constants were introduced and optimized in the process. The model was later found to behave poorly at low pressures[18,21] since corresponding tests had not been included in the validation database.

Katto (1990)[19] proposed a model based on a previous model by Haramura and Katto (1983)[22] for saturated pool boiling on an infinite horizontal flat plate. In both models, the vapor blanket is continuously replenished by a large number of small vapor stems normal to the heated surface which originated from nucleate boiling. Hydrodynamic instabilities at both stems-sublayer and sublayer-blanket interfaces are considered. In flow boiling, the same vapor stem coverage area as used in pool boiling was assumed, while the effects of forced convection and subcooling were investigated. No supply liquid was included during the passage time of the vapor blanket. This model served as the basis for the prevailing thinning processes

in the recently developed transient CHF model.[1] However, the Katto model was determined to be incapable of predicting accurate CHF for cases in which the local void fraction in the near-wall bubbly layer exceeded 70%,[21] and the existence of the modeled vapor stems is under question due to lack of experimental evidence.

Celata et al. (1994)[23] followed the same procedure as in Lee and Mudawar[20] to calculate the vapor blanket thickness, length, and velocity. The authors assumed that the vapor blanket lied on the superheated layer boundary (i.e., it existed only in the near-wall region where the local liquid is superheated), a strong assumption which proved to be inapplicable to near-saturation or saturated applications. Also, the model remained deficient in predictions at low L/D or high-pressure conditions.[21]

Celata et al. (1999)[24] later proposed a simpler approach—the so-called superheated layer vapor replenishment model—which used the same assumptions and closures as in the previous model. According to the new approach, CHF should occur when the vapor blanket replenishes the superheated layer, coming into contact with the heated surface. The validation performance was similar to that using the previous model, and the superheated assumption was still defective in low subcooling cases.

Liu et al. (2000)[21] proposed a new approach to determine the vapor blanket velocity. As shown in Figure 6, besides the sublayer-blanket interface (interface I), the authors also investigated the right-hand interface (interface II) and proved that the two interface wavelengths were equal to the vapor blanket length if the vapor blanket is stable. The core region[a] void fraction was simplified as the channel-averaged void fraction (i.e., all bubbles were assumed to be in the core region), as the liquid sublayer and the vapor blanket were claimed to be very thin. This assumption clearly contradicts the theory of vapor removal limit and bubble crowding, in which most bubbles accumulate in the vicinity of the wall. Similarly, the model only focused on subcooled boiling.

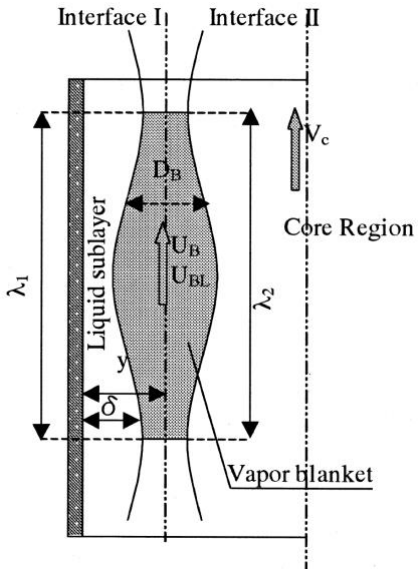

Figure 6. Schematic view of a stable vapor blanket in the Liu model.[21]

An improved, more realistic physics-based model combining the key components of the Liu model and the bubble crowding theory will be proposed. The new model will be optimized and validated with the round tube data as described in Section 2.2.

[a] Definition of the core region will be different in the proposed new model (Section 3.2).

3.2. New Model Description

Based on Lee and Mudawar,[20] DNB is triggered at the complete depletion of the liquid sublayer. Using heat balance, the CHF can be described as:

$$q''_{CHF} = \frac{\rho_f \delta [h_{fg} + c_1 C_{pl}(T_{sat} - T_{bulk})]}{L_B} U_B \quad (1)$$

where δ is the liquid sublayer thickness, and L_B and U_B denote the vapor blanket length and the velocity. The optimized empirical constant $c_1 = (T_{sat} - T_{supply})/(T_{sat} - T_{bulk}) = 0.35$, suggesting that the subcooling of the supply liquid is 35% of the bulk subcooling.[20] The sensitivity study reveals that the CHF is not sensitive to the value of c_1, and other papers[19,21-24] do not address the supply liquid component shown in Eq. (1). The liquid specific heat $C_{pl} \cong (C_{pf} + C_{p,supply})/2 \cong C_{pf}$.

Vapor blanket length L_B

As demonstrated in Liu et al.,[21] the vapor blanket length is equal to the same critical wavelength of the two interfaces, i.e.,

$$L_B = \lambda_1 = \lambda_2, \quad (2)$$

where λ_1 is the critical wavelength at interface I in Figure 6, which can be expressed as:

$$\lambda_1 = \frac{2\pi\sigma(\rho_f + \rho_g)}{\rho_f \rho_g (U_B - U_{sublayer})^2} \cong \frac{2\pi\sigma(\rho_f + \rho_g)}{\rho_f \rho_g {U_B}^2} \quad (3)$$

The thin liquid sublayer is attached to the wall and confined underneath the vapor blanket. Its average velocity can be neglected as compared to that of the vapor blanket. Similarly, the wavelength at interface II can be written as:

$$\lambda_2 = \frac{2\pi\sigma(\rho_2 + \rho_g)}{\rho_f \rho_g (U_2 - U_B)^2} = \frac{2\pi\sigma(\rho_b + \rho_g)}{\rho_f \rho_g (U_b - U_B)^2}, \quad (4)$$

where the subscript 2 under density and velocity denotes the local region on the right-hand side of interface II. As originally presented in Weisman and Pei's bubble crowding theory[25] and as illustrated in Figure 7, the flow channel in subcooled, or low-quality saturated boiling can be divided into two regions at near-CHF conditions: near-wall bubble region (or bubbly layer) and core region. As will be discussed later on the bubble region thickness, the local region 2 should fall within the bubble region (with subscript b).

From Eqs. (2)–(3), the calculation of L_B requires knowledge of the vapor blanket velocity, U_B.

Vapor blanket velocity U_B

Combining Eqs. (2)–(4), one can get:

$$U_B = \frac{U_b}{1 + \sqrt{\frac{\rho_f}{\rho_f + \rho_g} \frac{\rho_b + \rho_g}{\rho_b}}}, \quad (5)$$

where the mixture density in the bubble region ρ_b can be calculated from Eq. (6), assuming two-phase flow at thermal equilibrium (i.e., saturation):

$$\rho_b = \rho_g \alpha_b + \rho_f (1 - \alpha_b) \tag{6}$$

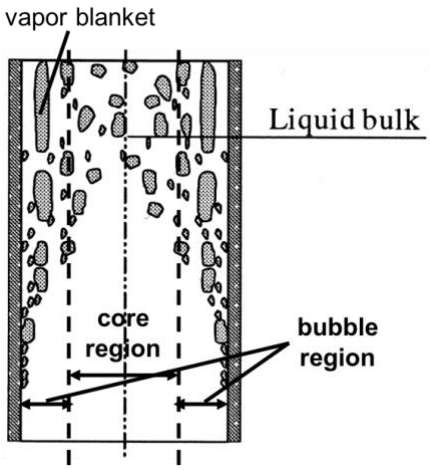

Figure 7. Schematic view of the flow channel in a round tube at near-CHF conditions.

The void fraction in bubble region α_b, also known as the *critical wall-void fraction*, is a key parameter inherent to the bubble crowding theory. Various values or data-fitting correlations have been attempted, comprising:

$\alpha_b =$	0.82	*by*	Weisman and Pei (1983)[25]
	0.75		Chang and Lee (1989)[26]
	function of local equilibrium quality		Kwon and Chang (1999)[27]
	0.8		Kodama and Kataoka (2003)[28]
			Vyskocil and Macek (2015)[29]
	function of pressure and local flow quality		Pan *et al.* (2016)[30]

At this point, there are not sufficient data[27] to accurately determine α_b, and as discussed in Kodama and Kataoka,[28] the predicted CHF should not be strongly dependent on this critical void value. To avoid introducing further empiricism and complexity to the model, its value is set as follows:

$$\alpha_b = 0.8 \tag{7}$$

Another key parameter in the bubble crowding theory is the bubble region thickness δ_b, which was also determined empirically by best-fitting to different datasets. It has been widely modeled as a constant multiplier of the bubble departure diameter D_d, i.e.:

$\delta_b = c_2 \cdot D_d$ where $c_2 =$	2.5	*by*	Weisman and Pei (1983)[25]
	1.7		Chang and Lee (1989)[26]
	1.0		Kwon and Chang (1999)[27]
	10.0		Yu and Zhang (2010)[31]

The multiplier c_2 was fitted with datasets at different operating conditions and different bubble departure diameter models. Based on the preliminary sensitivity work using Thompson's data from Table 1 and the modified-Staub bubble diameter model (detailed below), c_2 should mostly depend on the length-to-diameter ratio L/D, and it is optimized in the form of piecewise constants:

$$\delta_b = c_2 \cdot D_d, \tag{8}$$

$$\text{where } c_2 = \begin{cases} 10, & L/D \geq 100 \\ 8, & 75 \leq L/D < 100 \\ 6, & 50 \leq L/D < 75 \\ 3, & 25 \leq L/D < 50 \\ 1.5, & L/D < 25 \end{cases}$$

Bubble departure diameter D_d

The determination of the bubble departure diameter D_d is of high importance not only for δ_b, but also for the vapor blanket thickness (or equivalent diameter) D_B since $D_B \cong D_d$ was one of the basic assumptions in the liquid sublayer dryout theory. Its modeling has been the focus of numerous efforts over the past decades. Different semi-empirical or mechanistic models have been proposed, among which Levy (1967)[32] and Staub (1968)[33] have received special attention in the development of mechanistic DNB models.

The Levy approach was used in different CHF models such as Lee and Mudawar (1988),[20] Kwon and Chang (1999),[27] Liu et al. (2000),[21] Kinoshita et al. (2001),[34] and Yu and Zhang (2010).[31] As a semi-empirical model, it was based on the force balance (surface tension, drag, buoyancy) on a bubble in contact with the wall. It actually approximated D_d to the distance to the tip of the bubble and determined the leading coefficient using data calibration. This model is not adopted in this work because it would yield unrealistic values for c_2 and α_b.

The Staub approach was another semi-empirical model used for predicting CHF by authors such as Celata et al. (1994, 1999),[23,24] Kodama and Kataoka (2003),[28] and Pan et al. (2016).[30] This approach was also based on the force balance (surface tension, drag, buoyancy, bubble growth, lift) on a growing hemispherical shape bubble attached to the wall, and it can be expressed as:

$$D_d = \frac{32}{f}\frac{\sigma c_3 \rho_f}{G^2}, \tag{9}$$

where the friction factor f is calculated with the Colebrook-White equation[23] for tube applications,

$$\frac{1}{\sqrt{f}} = 1.14 - 2.0 log_{10}\left(\frac{\varepsilon}{D} + \frac{9.35}{Re\sqrt{f}}\right), \tag{10}$$

with the surface roughness, ε, to be in the order of the bubble diameter at departure, i.e., $\varepsilon \cong D_d$. As explained in Celata et al.,[23] the pressure drop gradient will rise at near-CHF conditions, as attached bubbles cause an increase in the surface roughness, but the coolant can still behave as single-phase liquid. D is the tube diameter, and Re is the channel Reynolds number calculated with saturated liquid properties. The empirical constant $c_3 = F_{surface\ tension}/(\pi D_d \sigma)$ was found to lie within the interval [0.015, 0.17] from pool boiling experiments with a contact angle between 20 and 70 degrees.[33] Staub also calibrated c_3 with some flow boiling water measurements and suggested a value of 0.02–0.03. Following the recommendation, Celata et al.[23,24] used c_3 = 0.03, whereas Pan et al.[30] used a much smaller value of

c_3 = 0.0075. Kodama and Kataoka[28] suggested that c_3 should vary widely according to the complicated local thermal-hydraulic conditions, so they introduced a linear function of subcooling (bounded by the maximum/minimum values from pool boiling validation by Staub), although no validation was performed, and the function was made up solely based on qualitative parametric trends. It is therefore worth optimizing this constant with Thompson tube CHF data[10] and developing a more reasonable piecewise constant function that varies with pressure P [MPa], mass flux G [kg/m^2-s], and exit equilibrium quality $x_{e,out}$ [-]. The optimized function for c_3 is presented in

Table **3**. The values are bounded within a reasonable interval and are in line with existing references.

Table 3. Optimized piecewise constant function for c_3 in Eq. (9).

	$G \geq 7000$	$5000 \leq G < 7000$	$3000 \leq G < 5000$	$2000 \leq G < 3000$	$1000 \leq G < 2000$	$500 \leq G < 1000$	$G < 500$
$P \geq 10$							
$x_{e,out} \geq 0.1$	–	0.120	0.075	0.040	0.030	0.015	0.006
$0.0 \leq x_{e,out} < 0.1$	0.150	0.070	0.055	0.035	0.020	0.012	0.005
$x_{e,out} < 0.0$	0.075	0.065	0.040	0.025	0.015	0.010	0.005
$3 \leq P < 10$							
$x_{e,out} \geq 0.1$	0.170	0.120	0.070	0.040	0.030	0.015	0.006
$0.0 \leq x_{e,out} < 0.1$	0.110	0.070	0.050	0.030	0.020	0.012	0.005
$x_{e,out} < 0.0$	0.075	0.060	0.035	0.025	0.015	0.010	0.005
$P < 3$							
$x_{e,out} \geq 0.1$	–	–	–	–	–	–	–
$0.0 \leq x_{e,out} < 0.1$	–	–	–	0.010	–	–	–
$x_{e,out} < 0.0$	–	0.010	0.010	–	–	–	–

Recent efforts in modeling the bubble departure diameter have focused on expanding and reevaluating the acting forces and have proposed more general formulas to calculate bubble diameter at departure to bulk or by sliding, as presented in the state-of-the-art model by Mazzocco et al.[35] However, such mechanistic models also required calibration to determine the bubble growth force; the reassessed buoyancy force would depend on both advancing and receding contact angles, for which very few data are available with large uncertainties. Further optimization work will be required, and such models were only validated against low mass flux, high subcooling data. At this point, no bubble diameter measurements are available at high pressure, high flow conditions. Moreover, in the proximity of CHF, the bubble size would not be exactly the same as those measured D_d, since bubbles are more likely to coalesce and form vapor slugs. For the purpose of this work, a bubble departure diameter model based on the work of Levy or Staub is deemed reasonable and appropriate.

Bubble region velocity U_b

Using Eqs. (8)–(10), one can calculate the bubble region thickness δ_b and then the fraction of the cross sectional area occupied by the core region, η_c, defined as:

$$\eta_c = \frac{A_c}{A} = \left(\frac{D-2\delta_b}{D}\right)^2 \quad \text{for tube applications,} \tag{11}$$

where A denotes the channel cross-sectional area. The void fraction and density in the core region, α_c and ρ_c, can be calculated from:

$$\alpha_c = \frac{\alpha_{out}}{\eta_c} - \frac{\alpha_b(1-\eta_c)}{\eta_c} \tag{12}$$

$$\rho_c = \rho_g \alpha_c + \rho_{l,out}(1-\alpha_c), \tag{13}$$

where the channel-averaged outlet void fraction, α_{out}, can be obtained from subchannel codes (e.g., CTF, VIPRE-01) or from a commonly used drift-flux approach such as Chexal-Lellouche,[36] which requires the exit/local flow quality (x_{out}) information. x_{out} can be determined from subchannel analysis results or by using the well-accepted Levy[32] or Saha and Zuber[37] model. Assuming homogeneous flow in the core region,[27,31] the exit core region quality x_c turns to

$$x_c = \frac{\rho_g \alpha_c}{\rho_c} \tag{14}$$

The total liquid mass flow rate, $\dot{m}_l$, is written as:

$$\dot{m}_l = \dot{m}(1-x_{out}) = GA(1-x_{out}) \tag{15}$$

In order to calculate the liquid mass flow rate in each region, one may start with the average liquid velocity in the bubble region, $\bar{U}_{bl}$. This can be done by assuming that liquid within the bubbly layer follows the Karman velocity distribution, originally developed for single-phase turbulent flow, i.e.,

$$U_{bl}^+ = \begin{cases} y^+, & 0 \le y^+ < 5 \\ 5.0lny^+ - 3.05, & 5 \le y^+ < 30, \\ 2.5lny^+ + 5.5, & y^+ \ge 30 \end{cases} \tag{16}$$

where $U_{bl}^+ = U_{bl}/U_\tau$, $U_\tau = \sqrt{\tau_w/\rho_f}$, $y^+ = yU_\tau\rho_f/\mu_f$, $\tau_w = fG^2/(8\rho_f)$. Hence, the average velocity becomes

$$\bar{U}_{bl} = \bar{U}_{bl}^+ \cdot U_\tau \tag{17}$$

and

$$\bar{U}_{bl}^+ = \begin{cases} \frac{1}{y_{\delta_b}^+}\int_0^{y_{\delta_b}^+} y^+ dy^+, & 0 \le y_{\delta_b}^+ < 5 \\ \frac{1}{y_{\delta_b}^+}\left[\int_0^5 y^+ dy^+ + \int_5^{y_{\delta_b}^+}(5lny^+ - 3.05)dy^+\right], & 5 \le y_{\delta_b}^+ < 30, \\ \frac{1}{y_{\delta_b}^+}\left[\int_0^5 y^+ dy^+ + \int_5^{30}(5lny^+ - 3.05)dy^+ + \int_{30}^{y_{\delta_b}^+}(2.5lny^+ + 5.5)dy^+\right], & y_{\delta_b}^+ \ge 30 \end{cases} \tag{18}$$

with $y_{\delta_b}^+ = \delta_b U_\tau \rho_f/\mu_f$.

Once $\bar{U}_{bl}$ is known, one can calculate the liquid mass flow rate in the bubble region, $\dot{m}_{bl}$, as

$$\dot{m}_{bl} = \rho_f \bar{U}_{bl} A_{bl} = \rho_f \bar{U}_{bl} A_b(1-\alpha_b) = \rho_f \bar{U}_{bl} A(1-\eta_c)(1-\alpha_b), \tag{19}$$

and the liquid mass flow rate in the core region, $\dot{m}_{cl}$, from Eqs. (15) and (19):

$$\dot{m}_{cl} = \dot{m}_l - \dot{m}_{bl} \tag{20}$$

Then, the total mass flow rate in the core region is

$$\dot{m}_c = \rho_c U_c A \eta_c, \tag{21}$$

where

$$U_c = U_{cl} = U_{cv} = \frac{\dot{m}_{cl}}{\rho_{l,out} A_{cl}} = \frac{\dot{m}_{cl}}{\rho_{l,out} A \eta_c (1-\alpha_c)} \quad \text{(homogeneous flow)}, \tag{22}$$

and the total mass flow rate in the bubble region is

$$\dot{m}_b = \dot{m} - \dot{m}_c = GA - \dot{m}_c \tag{23}$$

The exit bubble region quality x_b turns to

$$x_b = \frac{\dot{m}_{bv}}{\dot{m}_b} = 1 - \frac{\dot{m}_{bl}}{\dot{m}_b} \tag{24}$$

Finally, the bubble region (average) velocity, U_b, can be expressed by

$$U_b = \frac{\dot{m}_b}{\rho_b A (1-\eta_c)} = \frac{G(x_{out} - x_c)}{\rho_b (x_b - x_c)(1-\eta_c)} \tag{25}$$

Liquid sublayer thickness δ

As illustrated in Figure 6, the liquid sublayer thickness δ is approximately the difference between the distance from the wall to the bubble centerline y and one half of the vapor blanket thickness D_B, i.e.,

$$\delta = y - D_B/2 = y - D_d/2 \tag{26}$$

Making use of Eq. (16), one can obtain

$$y = \frac{\mu_f}{U_\tau \rho_f} \cdot \begin{cases} U_{Bl}^+, & 0 \le U_{Bl}^+ < 5 \\ \exp[(U_{Bl}^+ + 3.05)/5], & 5 \le U_{Bl}^+ < 13.96, \\ \exp[(U_{Bl}^+ - 5.5)/2.5], & U_{Bl}^+ \ge 13.96 \end{cases} \tag{27}$$

where $U_{Bl}^+ = U_{Bl}/U_\tau$, and U_{Bl} is the liquid velocity at the vapor blanket centerline. The latter is calculated via a force balance on the vapor blanket between buoyancy and drag forces and can be arranged as

$$U_{Bl} = U_l\left(y = \delta + \frac{D_B}{2}\right) = U_B - \left(\frac{2L_B g(\rho_f - \rho_g)}{\rho_f C_D}\right)^{0.5}, \tag{28}$$

where U_B and L_B come from Eqs. (5) and (2), respectively, and the drag coefficient C_D can be obtained by either Harmathy (if exit pressure is smaller than 1 MPa) or Chan and Prince (otherwise).[21]

In Eqs. (1)–(28), the CHF can be predicted by an iterative procedure for any given channel geometry[a] and flow conditions.

[a] Some of the closures need to be further modified for non-tube applications.

3.3. Model Evaluation

As summarized in Table 4 and plotted in Figure 8, the improved new model is compared to the 2006 look-up table,[3] the Liu model,[21] and the best-estimate NN 10-fold cross-validation result (Section 2.3, from all data) against the 1,439 tube test cases (as listed in **Error! Reference source not found.**). For most selected datasets, the new model is significantly better than Liu, one of the relatively successful mechanistic models thus far. It outperforms cross-validated NN and is in line with the solely data-mapped look-up table. With the new model, 92% of test cases are predicted within ±20% uncertainty range (98% within ±30% uncertainty).

When compared to experimental data, the relative errors of the predicted CHF are assessed in Figures 9–13. It is important to note that the new model has demonstrated unbiased close agreement with measurements over the entire ranges of interest (pressure, mass flux, equilibrium quality, tube diameter, and length-to-diameter ratio) and has generally showed less scatter than the other predictive tools. As discussed in Section 3.1 and as illustrated in Figure 11 from the Liu results, most existing physics-based models only considered subcooled boiling, and their assumptions might not be valid for low subcooling or saturated flow cases.

Table 4. Predicted tube SS CHF performance with different models.

Tube dataset	# data	Look-up table rRMSE	Look-up table within 20% error	Liu rRMSE	Liu within 20% error	NN rRMSE	NN within 20% error	New model rRMSE	New model within 20% error
Inasaka	7	0.31	43%	0.18	71%	0.29	29%	0.20	71%
Peskov	17	0.10	94%	0.14	94%	0.47	29%	0.11	100%
Thompson	1,202	0.12	94%	0.32	52%	0.13	92%	0.12	91%
Weatherhead	162	0.05	100%	0.18	75%	0.09	99%	0.09	98%
Williams	51	0.04	100%	0.21	63%	0.14	84%	0.11	90%
Total	**1,439**	**0.12**	**95%**	**0.30**	**56%**	**0.14**	**92%**	**0.12**	**92%**

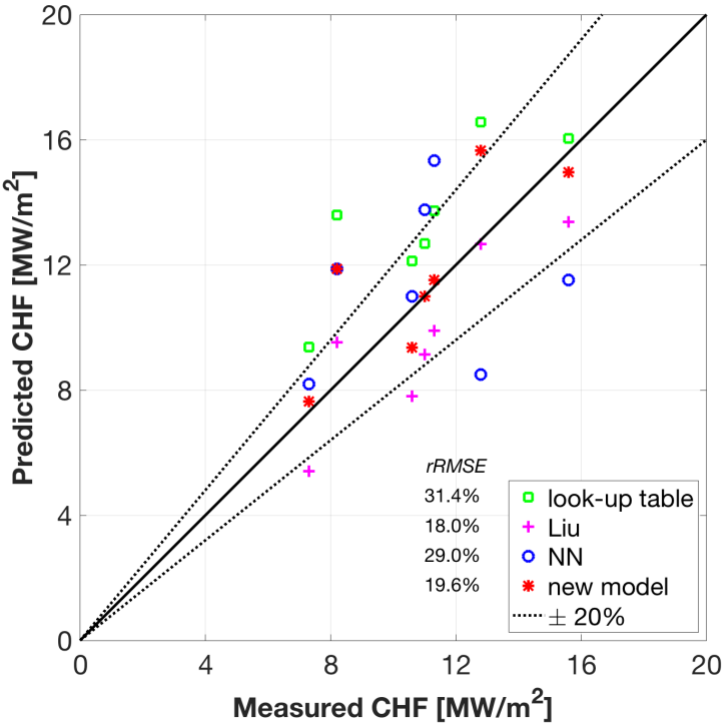

(a) Inasaka data

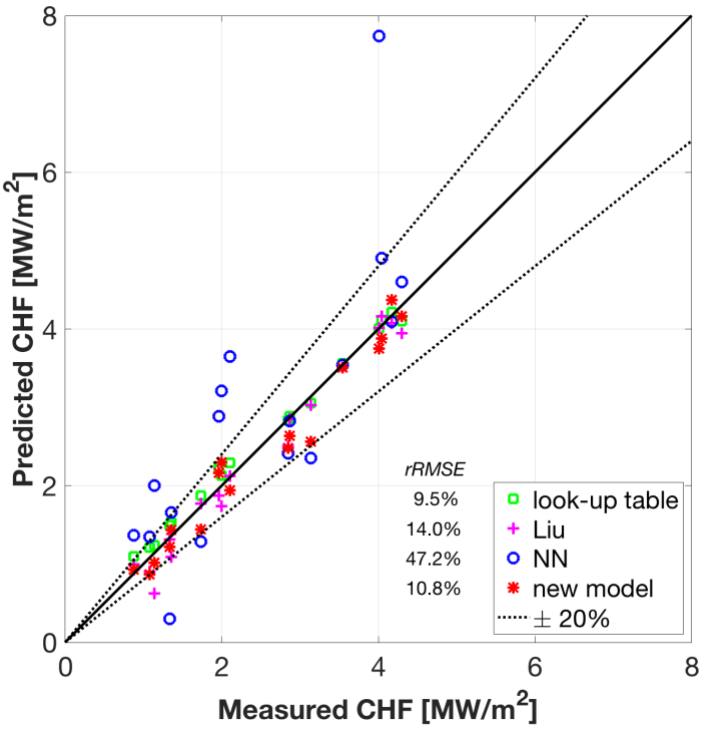

(b) Peskov data

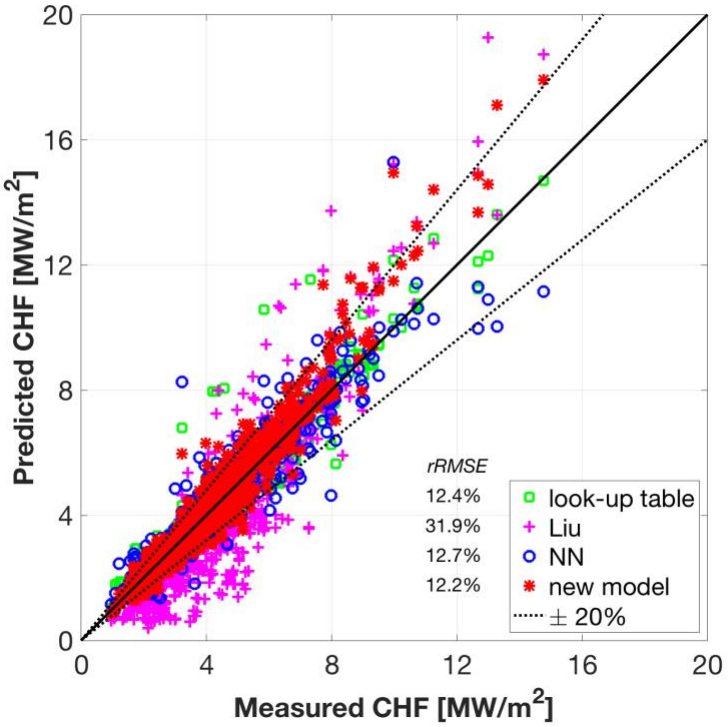

(c) Thompson data[a]

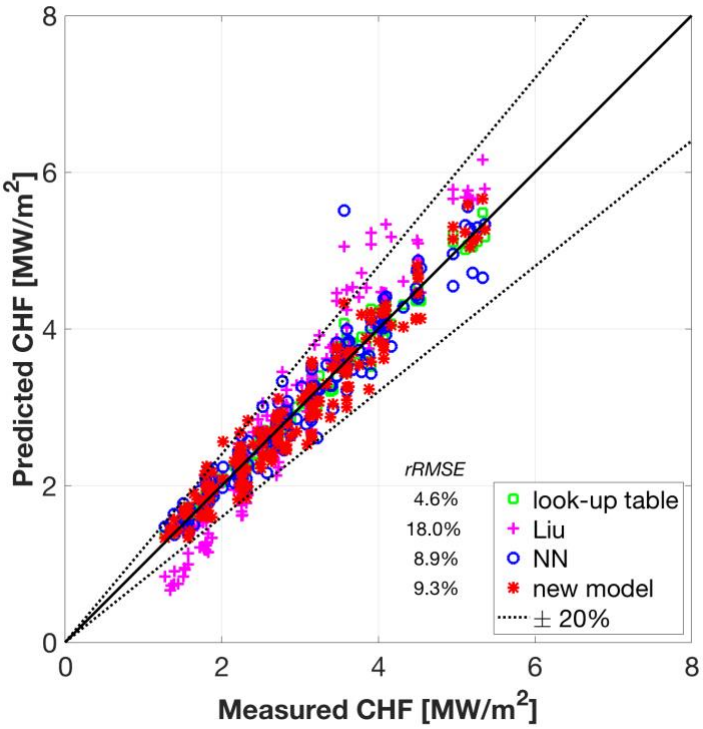

(d) Weatherhead data

[a] For the selected Thompson dataset, 72 out of 1,439 cases failed to converge using the Liu model.

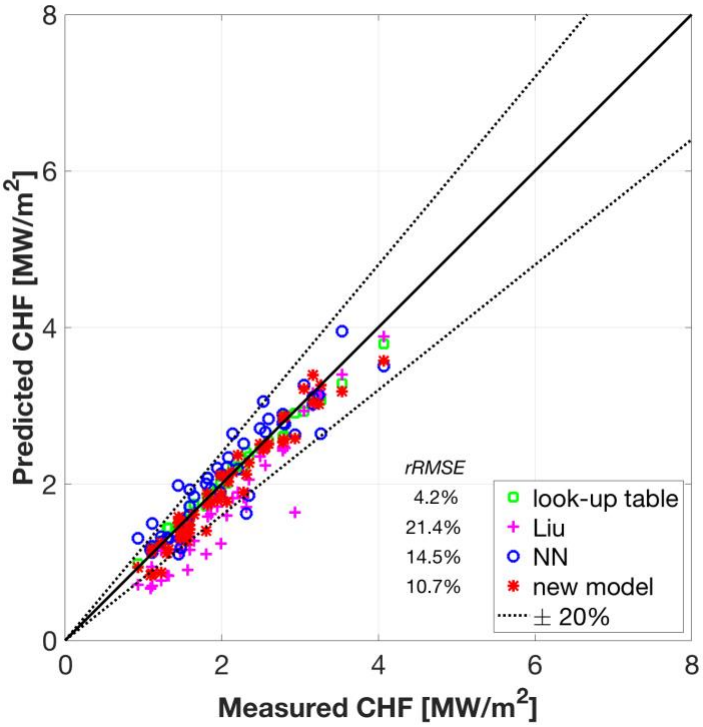

(e) Williams data

Figure 8. Predicted vs. measured tube CHF with look-up table, Liu model, best-estimate NN (10-fold), and new model.

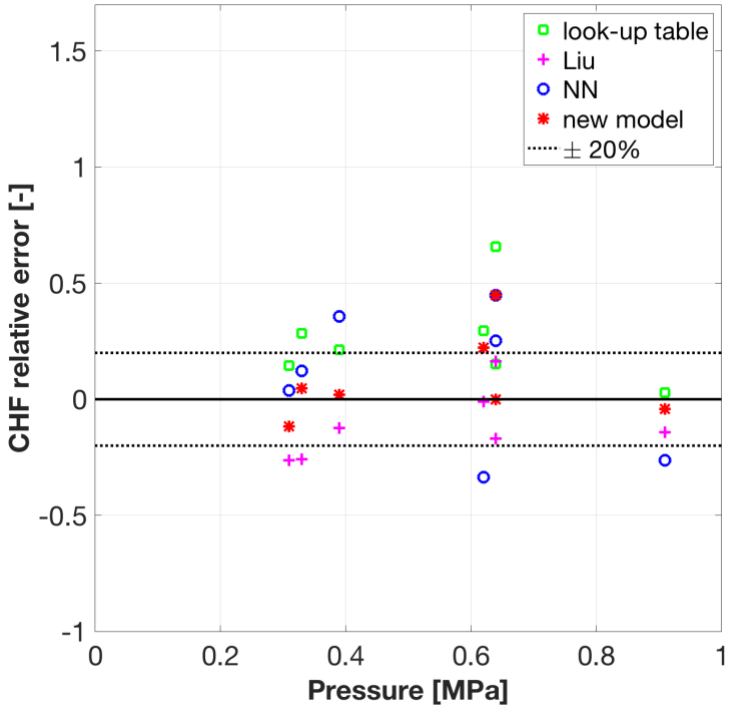

(a) Inasaka data

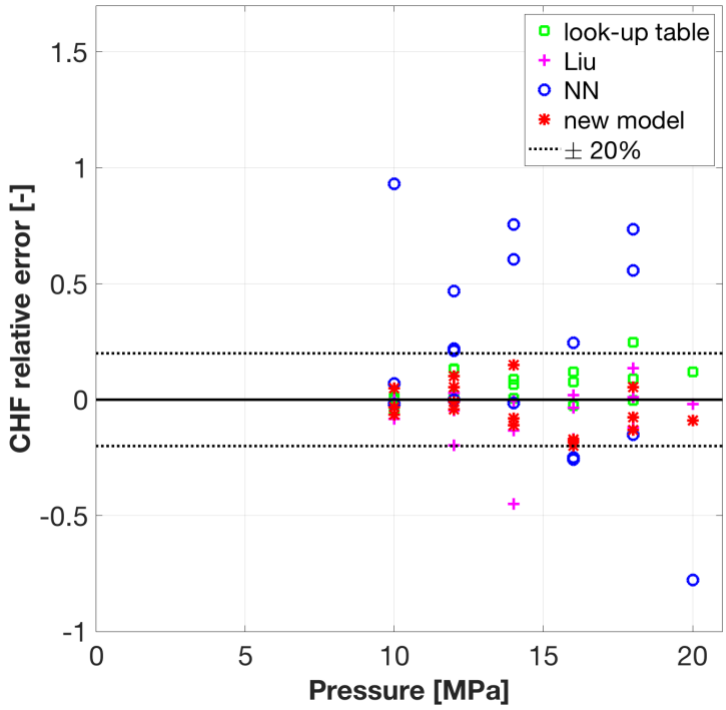

(b) Peskov data

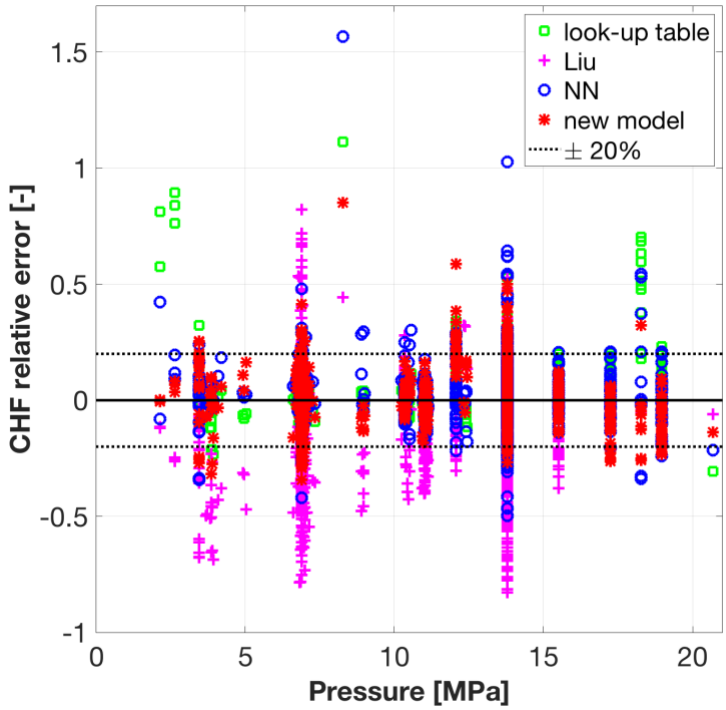

(c) Thompson data

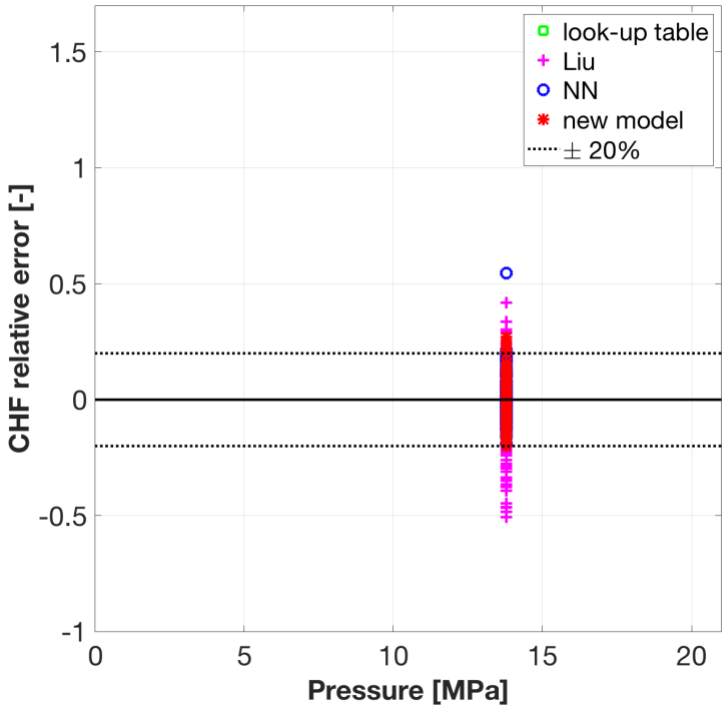

(d) Weatherhead data

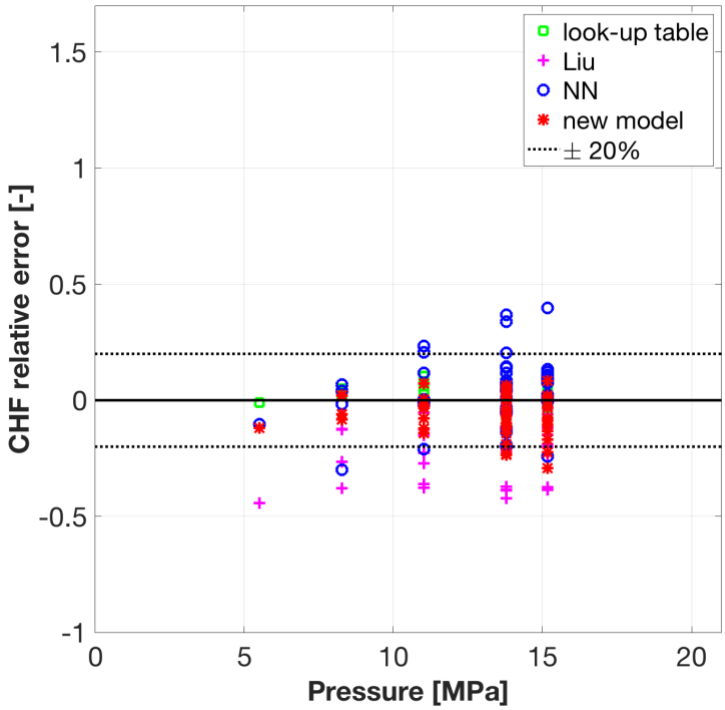

(e) Williams data

Figure 9. Tube CHF relative error vs. pressure.

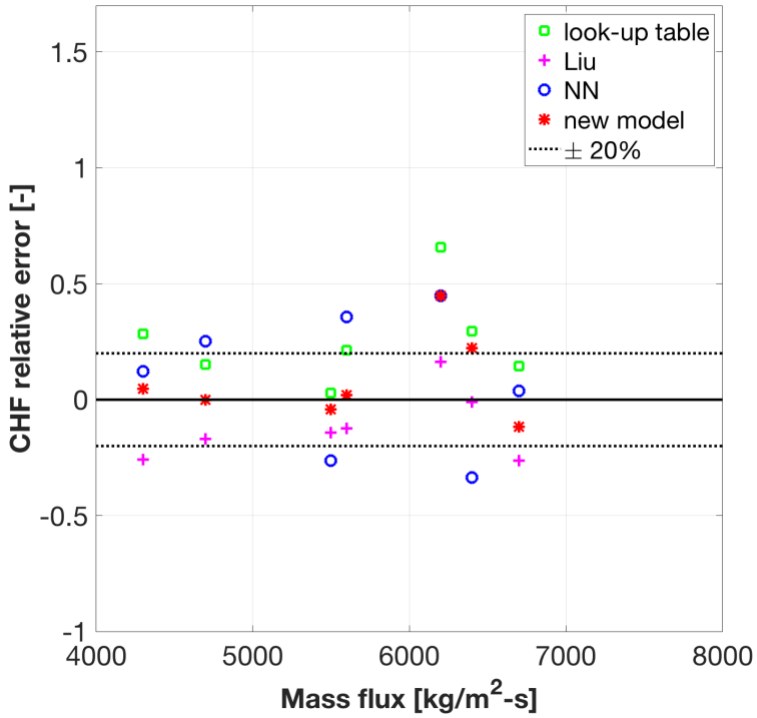

(a) Inasaka data

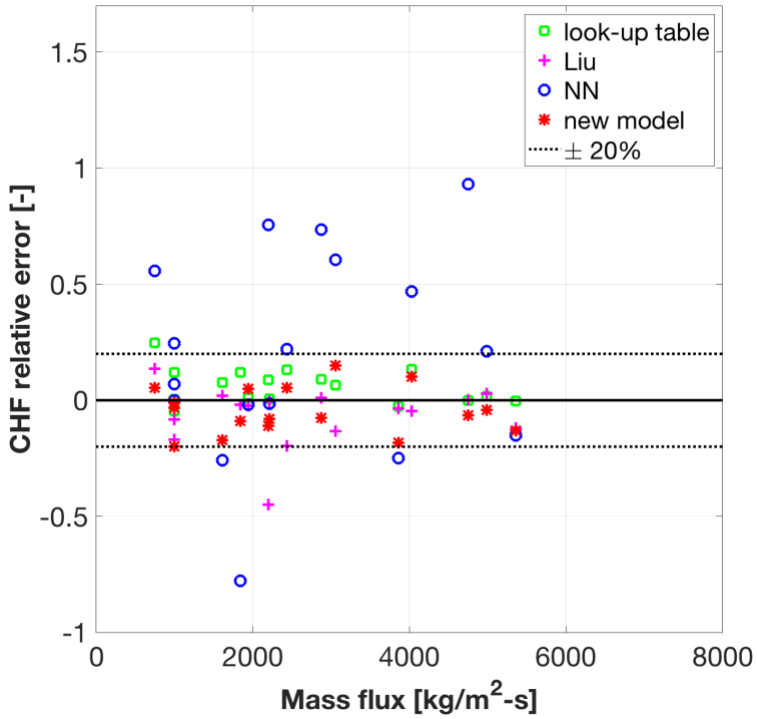

(b) Peskov data

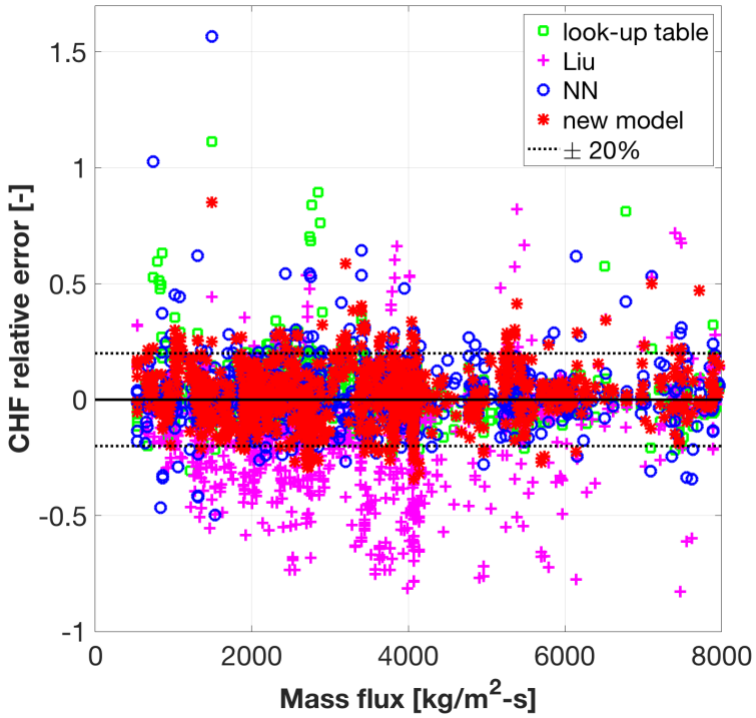

(c) Thompson data

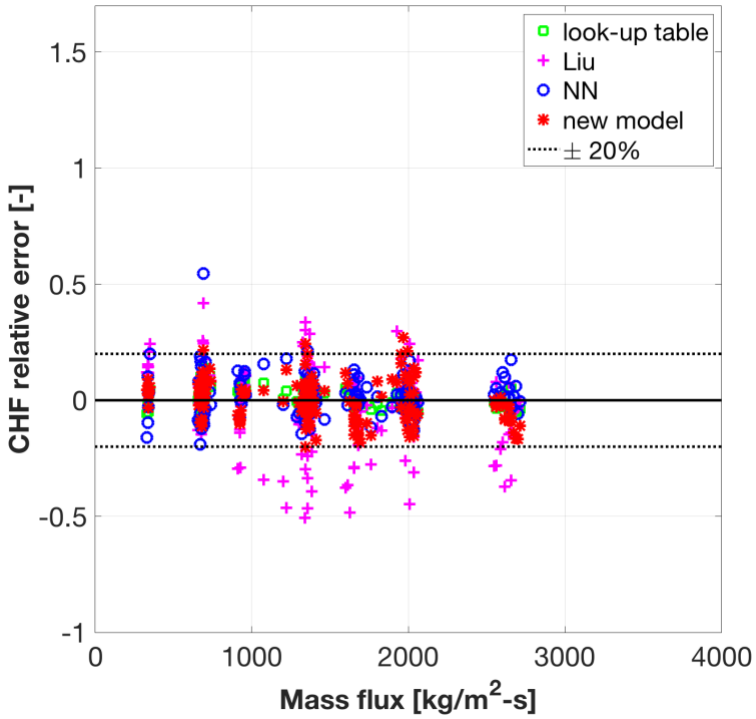

(d) Weatherhead data

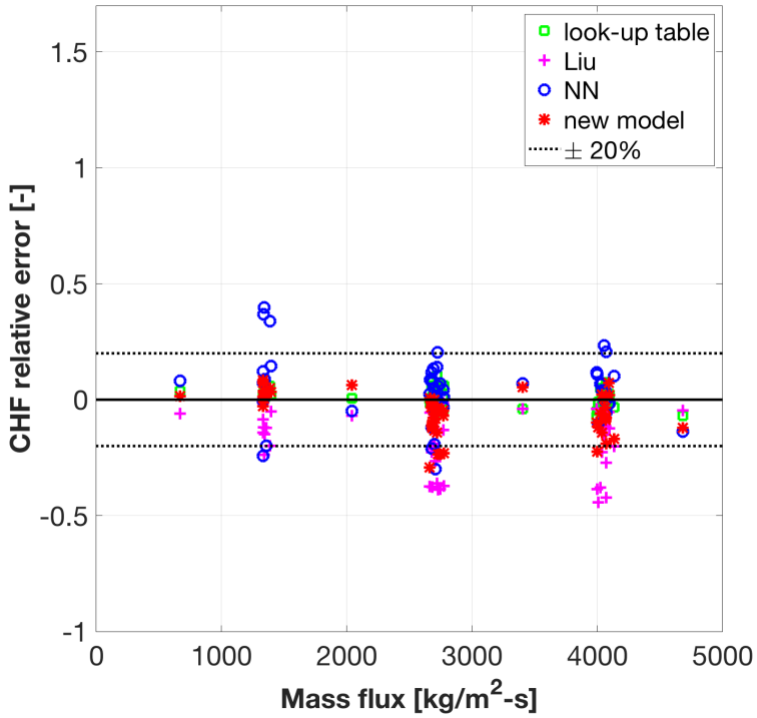

(e) Williams data

Figure 10. Tube CHF relative error vs. mass flux.

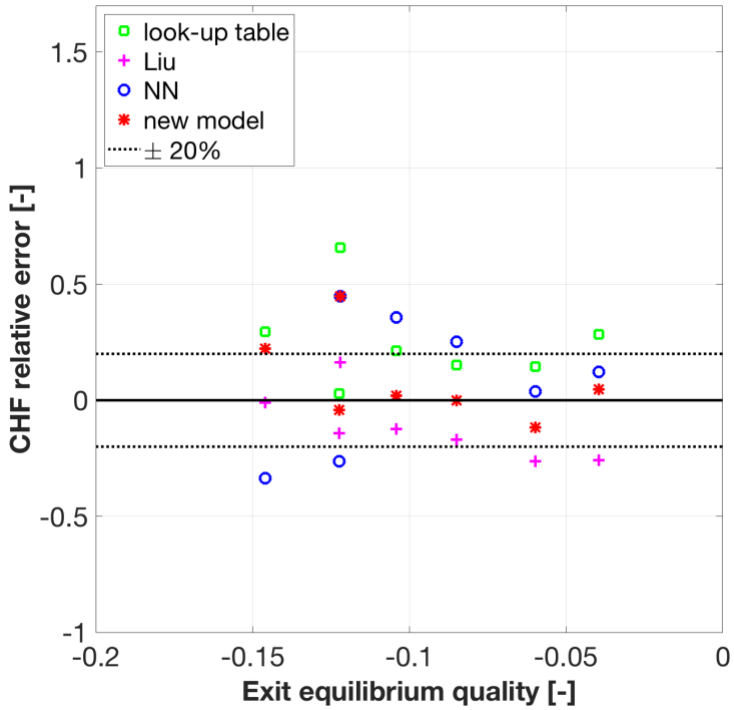

(a) Inasaka data

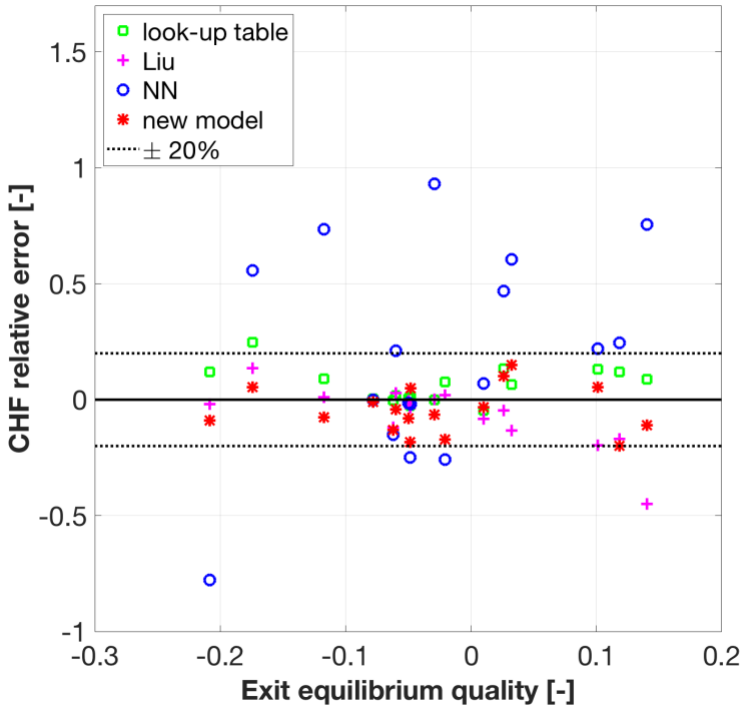

(b) Peskov data

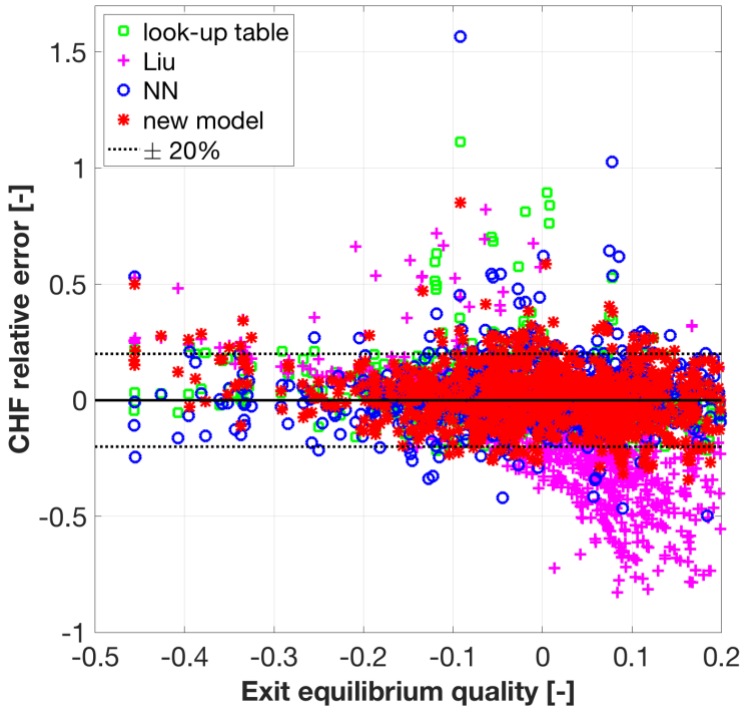

(c) Thompson data

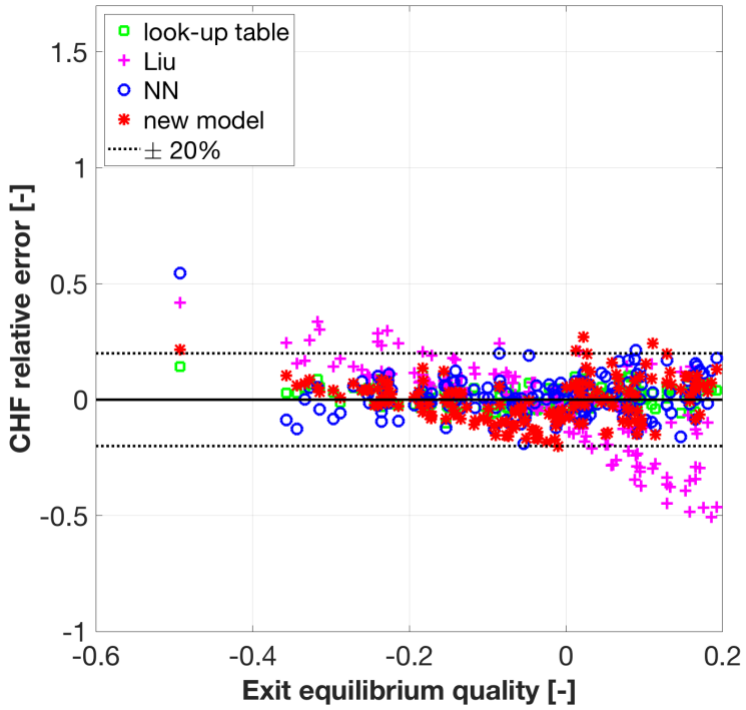

(d) Weatherhead data

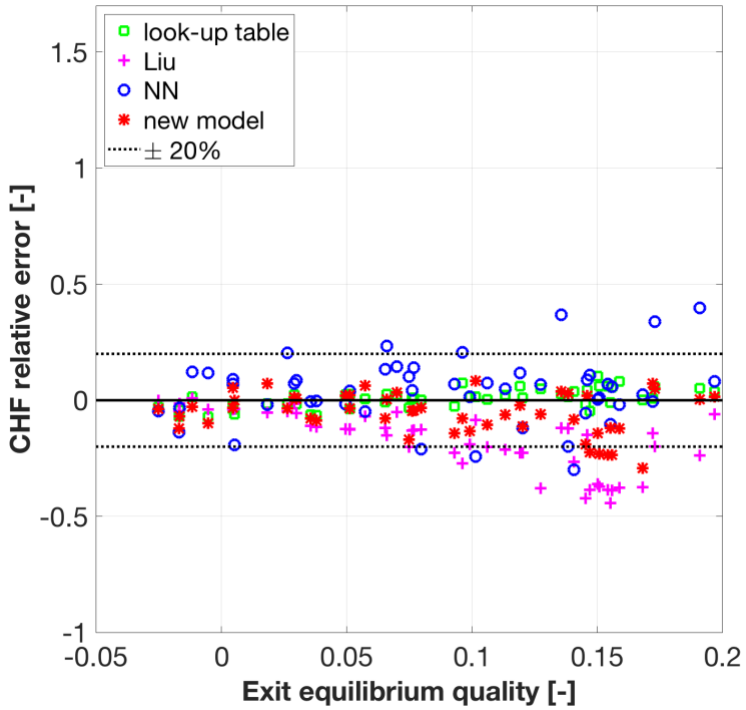

(e) Williams data

Figure 11. Tube CHF relative error vs. exit equilibrium quality.

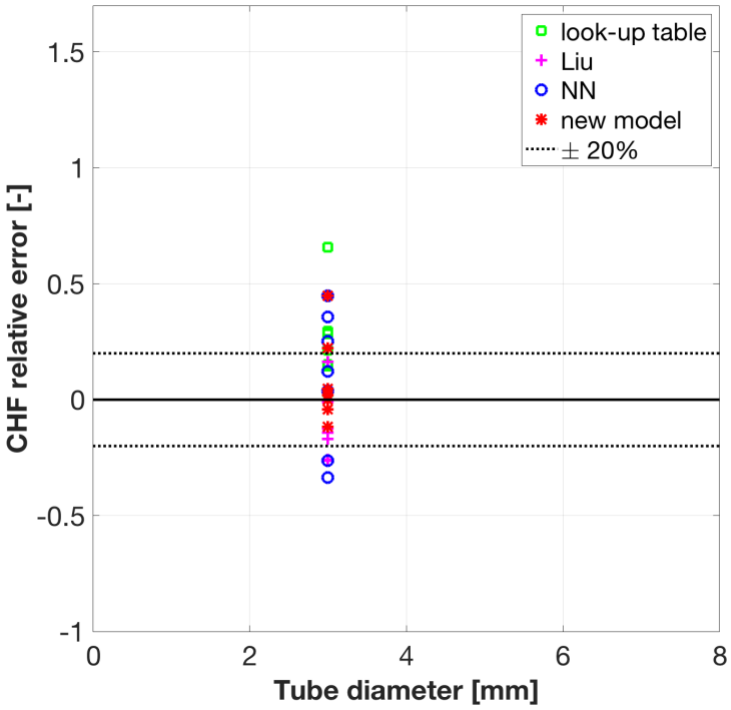

(a) Inasaka data

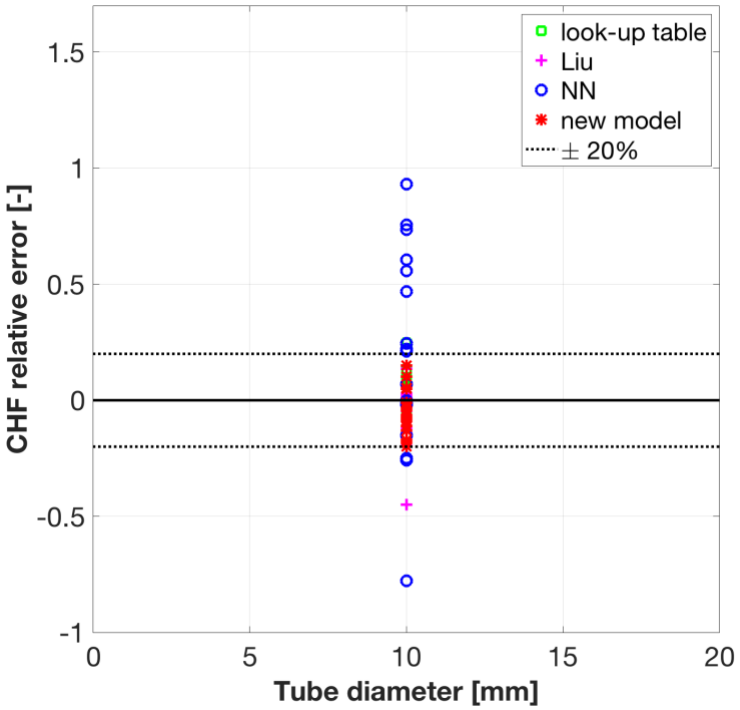

(b) Peskov data

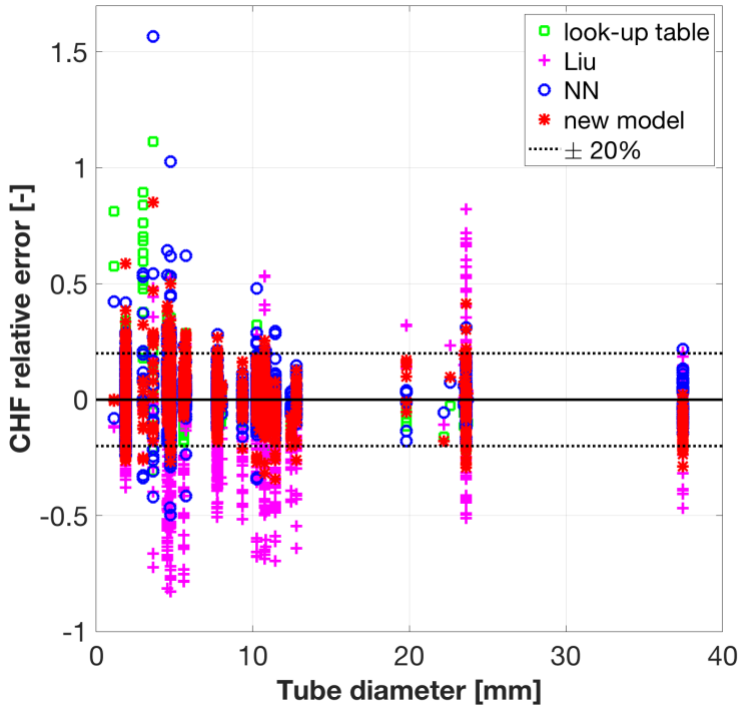

(c) Thompson data

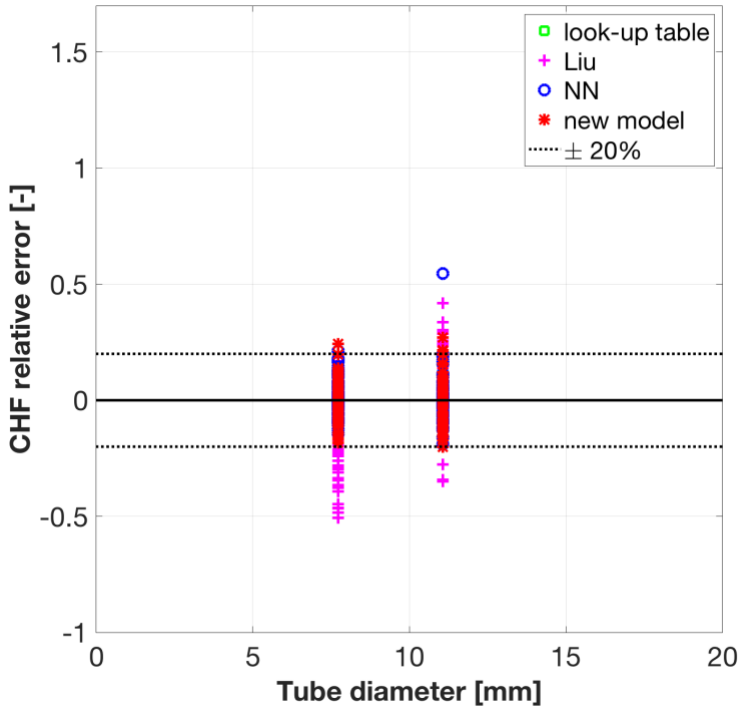

(d) Weatherhead data

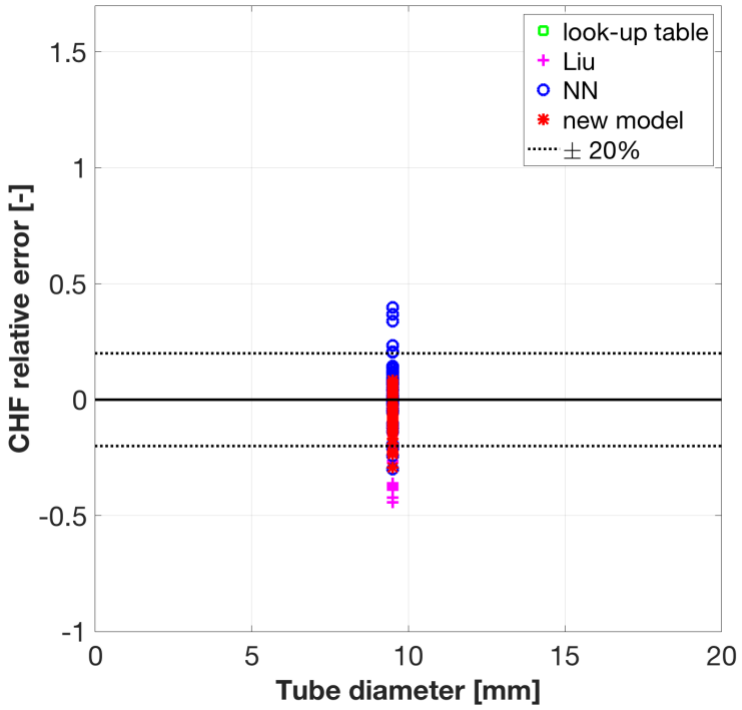

(e) Williams data

Figure 12. Tube CHF relative error vs. tube diameter.

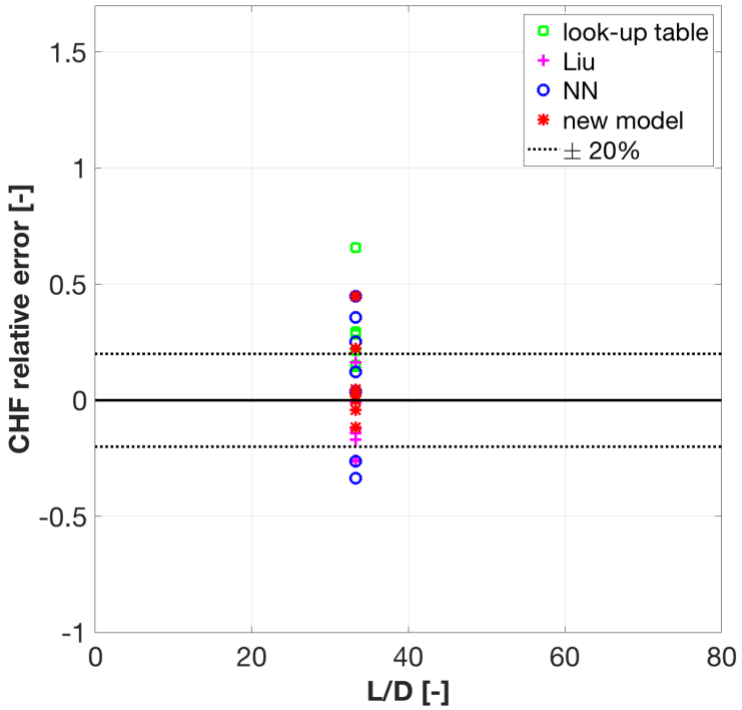

(a) Inasaka data

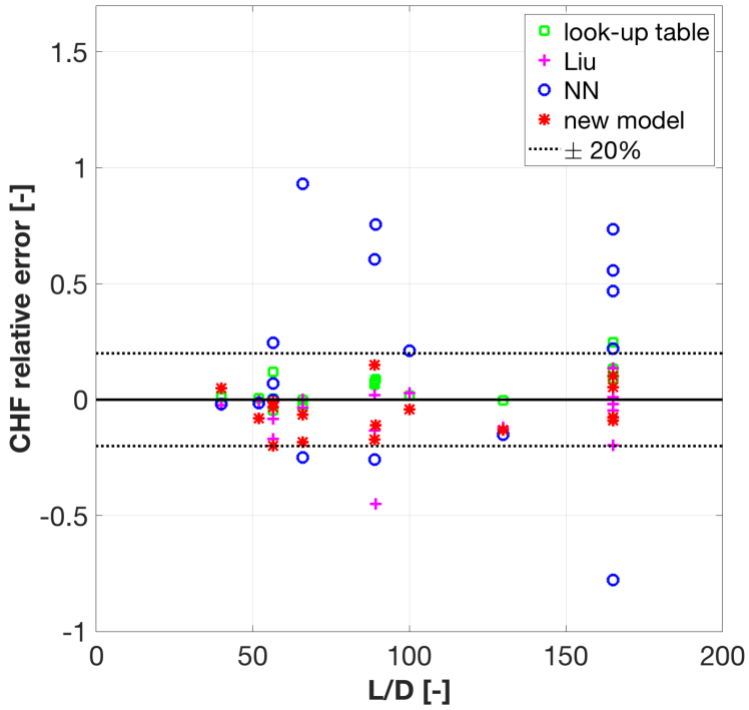

(b) Peskov data

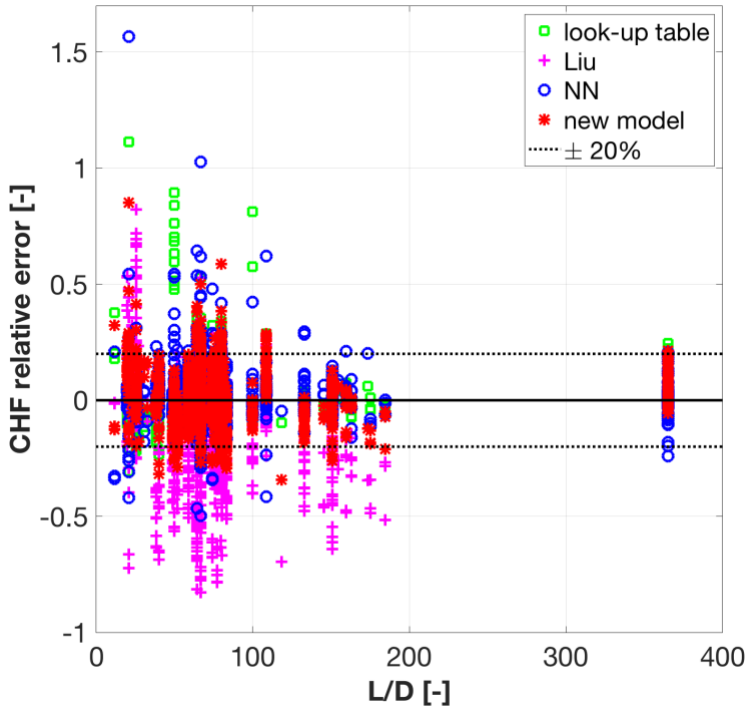

(c) Thompson data

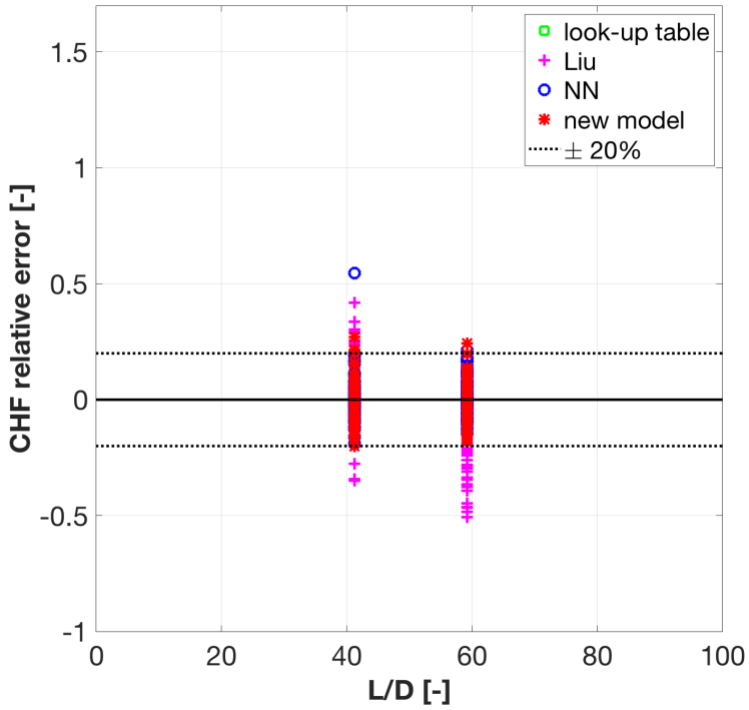

(d) Weatherhead data

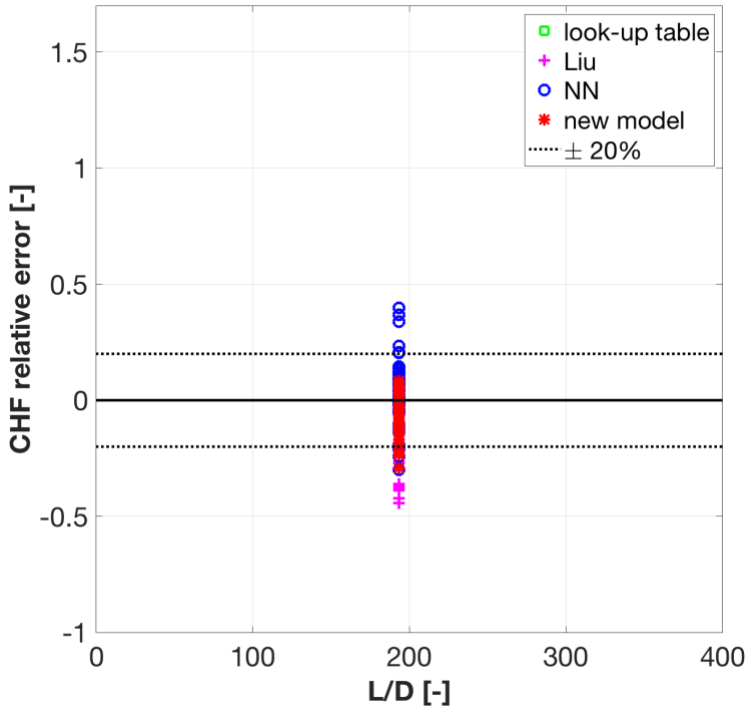

(e) Williams data

Figure 13. Tube CHF relative error vs. length-to-diameter ratio.

4. CONCLUSIONS AND FUTURE WORK

This report extends the predictive capabilities of data- and physics-driven tools for steady-state DNB-type CHF by developing two advanced approaches and providing insight into further improvements of the transient CHF model.

The proposed data-driven approach consists of using deep feed-forward NN and tree-based RF to cross-validate with 1,865 CHF test cases, covering a wide range of flow conditions and channel geometries. The best-estimate ML-based predictors compare favorably with the widely used look-up table for annulus and plate, and sensitivity analysis has confirmed their effectiveness. The key advantage of ML-based methods is their online extensibility of applicability domain. Changing from local quality to inlet subcooling in the input features yields even better agreement with measurements. In terms of computational time, for a single evaluation of all 1,865 data points on a personal computer, RF runs the fastest (< 1s), while NN (1–2 min) is slightly slower than the look-up table.

The proposed physics-driven approach has combined key assumptions and parameters in the state-of-the-art mechanistic theories of liquid sublayer dryout and near-wall bubble crowding. A more realistic understanding of local mechanisms has been modeled. The new model has been optimized and validated against 1,439 tube data, showing considerably improved performance as compared to one of the recent mechanistic models. It has demonstrated unbiased close agreement with measurements over the selected wide range of operating conditions.

The next step will extend the improved physics-driven model to non-tube geometry applications. More experimental data will be the key to a more deeply optimized predictive tool. With a larger database, a thorough process for training, validation, and testing may be permitted for ML-based methods. Their input features will be increased or modified further if other channel geometries are considered. For instance, with rod bundle data, one may need to include bundle-specific features such as spacer grids and nonuniform power distribution, as well as local flow conditions with the help of subchannel tools like CTF. Future work will also couple physics-based models (or table methods) and ML by means of a hybrid grey-box approach.[38] Residuals by the mechanistic (or table) CHF predictors will be added into the input feature vector, and the NN will be trained, along with other features of interest. In this way, the NN will work to pick up any additional (undiscovered) dependencies between the input features and will be guaranteed to perform at least as well as the standalone mechanistic/table approach or the traditional black-box NN.

Finally, the transient CHF model will be further improved based on the steady-state progress. Depending on the applications of interest, a new SS model (data-driven, physics-driven, or blended) may be implemented in CTF. Its solution will serve to be the starting point of the liquid sublayer thickness evaluation in the transient model. The advanced physics-driven approach will help advance understanding and model the DNB triggering mechanisms at different geometry and flow conditions under time-dependent scenarios. Ultimately, full-core RIA simulations will be performed with CTF to demonstrate the usefulness of the improved model.

ACKNOWLEDGMENTS

The author would like to acknowledge support from CASL for the completion of this milestone work, with special thanks to Dr. Robert K. Salko (ORNL) and Dr. Aaron J. Wysocki (ORNL), as well as Prof. Koroush Shirvan (MIT).

REFERENCES

1. X. Zhao, A. J. Wysocki, R. K. Salko, and K. Shirvan, "Mechanistic Modeling of Departure from Nucleate Boiling under Transient Scenarios," *Proc. of the International Congress on Advances in Nuclear Power Plants* (*ICAPP*), Charlotte, NC, USA (2018).

2. A. Kossolapov, G. Su, T. McKrell, M. Bucci, and J. Buongiorno, "Transient Flow Boiling and CHF under Exponentially Escalating Heat Inputs," *Proc. of the 17th International Topical Meeting on Nuclear Reactor Thermal Hydraulics* (*NURETH-17*), Xi'an, China, September 3–8 (2017).

3. D. C. Groeneveld, J. Q. Shan, A. Z. Vasic, L. K. H. Leung, A. Durmayaz, J. Yang, S. C. Cheng, and A. Tanase, "The 2006 CHF Look-Up Table," *Journal of Nuclear Engineering and Design*, 237, 1909–1922 (2007).

4. A. S. Nafey, "Neural Network Based Correlation for Critical Heat Flux in Steam-Water Flows in Pipes," *International Journal of Thermal Sciences*, 48, 2264–2270 (2009).

5. S. K. Moon, W. P. Baek, and S.H. Chang, "Parametric Trends Analysis of the Critical Heat Flux Based on Artificial Neural Networks," *Journal of Nuclear Engineering and Design*, 163, 29–49 (1996).

6. G. Su, K. Fukuda, D. Jia, and K. Morita, "Application of an Artificial Neural Network in Reactor Thermohydraulic Problem: Prediction of Critical Heat Flux," *Journal of Nuclear Science and Technology*, 39(5), 564–571 (2002).

7. T. Cong, G. Su, S. Qiu, and W. Tian, "Applications of ANNs in Flow and Heat Transfer Problems in Nuclear Engineering: A Review Work," *Progress in Nuclear Energy*, 62, 54–71 (2013).

8. F. Inasaka and H. Nariai, "Critical Heat Flux of Subcooled Flow Boiling for Water in Uniformly Heated Straight Tubes," *Journal of Fusion Engineering and Design*, 19, 329–337 (1992).

9. O. L. Peskov, V. I. Subbotin, B. A. Zenkevich, and N. D. Sergeyev, "The Critical Heat Flux for the Flow of Steam-Water Mixtures through Pipes," Pergamon Press, Kutateladze (1969).

10. B. Thompson and R. V. Macbeth, "Boiling Water Heat Transfer Burnout in Uniformly Heated Round Tubes: A Compilation of World Data with Accurate Correlations," AEEW-R356 (1964).

11. R. J. Weatherhead, "Nucleate Boiling Characteristics and the Critical Heat Flux Occurrence in Subcooled Axial-Flow Water Systems," ANL-6675 (1963).

12. C. L. Williams and S. G. Beus, "Critical Heat Flux Experiments in a Circular Tube with Heavy Water and Light Water," WAPD-TM-1462 (1980).

13. S. G. Beus and O. P. Seebold, "Critical Heat Flux Experiments in an Internally Heated Annulus with a Non-Uniform, Alternate High and Low Axial Heat Flux Distribution," WAPD-TM-1475 (1981).

14. E. Janssen and J. A. Kervinen, "Burnout Conditions for Single Rod in Annular Geometry, Water at 600 to 1400 psia," GEAP-3899 (1963).

15. E. P. Mortimore and S. G. Beus, "Critical Heat Flux Experiments with a Local Hot Patch in an Internally Heated Annulus," WAPD-TM-1419 (1979).

16. A. J. Richenderfer, "Experimental Study of Heat Flux Partitioning in Pressurized Subcooled Flow Boiling," PhD thesis, MIT (2017).

17. X. Zhao, "Prediction of Steam-Water Flow Boiling Critical Heat Flux in Tubes and Annuli using Physics-Informed Deep Feed-Forward Neural Networks," project technical report, www.researchgate.net/publication/326782411 (2018).

18. M. Bruder, G. Bloch, and T. Sattelmayer, "Critical Heat Flux in Flow Boiling - Review of the Current Understanding and Experimental Approaches," *Heat Transfer Engineering*, 38(3), 347–360 (2017).

19. Y. Katto, "A Physical Approach to Critical Heat Flux of Subcooled Flow Boiling in Round Tubes," *International Journal of Heat and Mass Transfer*, 33(4), 611–620 (1990).

20. C. H. Lee and I. Mudawar, "A Mechanistic Critical Heat Flux Model for Subcooled Flow Boiling Based on Local Bulk Flow Conditions," *International Journal of Multiphase Flow*, 14(6), 711–728 (1988).

21. W. Liu, H. Nariai and F. Inasaka, "Prediction of Critical Heat Flux for Subcooled Flow Boiling," *International Journal of Heat and Mass Transfer*, 43, 3371–3390 (2000).

22. Y. Haramura and Y. Katto, "A New Hydrodynamic Model of Critical Heat Flux, Applicable Widely to Both Pool and Forced Convection Boiling on Submerged Bodies in Saturated Liquids," *International Journal of Heat and Mass Transfer*, 26(3), 389–399 (1983).

23. G. P. Celata, M. Cumo, A. Mariani, M. Simoncini, and G. Zummo, "Rationalization of Existing Mechanistic Models for the Prediction of Water Subcooled Flow Boiling Critical Heat Flux," *International Journal of Heat and Mass Transfer*, 37(1), 347–360 (1994).

24. G. P. Celata, M. Cumo, Y. Katto, and A. Mariani, "Prediction of the Critical Heat Flux in Water Subcooled Flow Boiling using a New Mechanistic Approach," *International Journal of Heat and Mass Transfer*, 42, 1457–1466 (1999).

25. J. Weisman and B. S. Pei, "Prediction of Critical Heat Flux in Flow Boiling at Low Qualities," *International Journal of Heat and Mass Transfer*, 26(10), 1463–1477 (1983).

26. S. H. Chang and K. W. Lee, "A Critical Heat Flux Model Based on Mass, Energy and Momentum Balance for Upflow Boiling at Low Qualities," *Journal of Nuclear Engineering and Design*, 113, 35–50 (1989).

27. Y. M. Kwon and S. H. Chang, "A Mechanistic Critical Heat Flux Model for Wide Range of Subcooled and Low-Quality Flow Boiling," *Journal of Nuclear Engineering and Design*, 188, 27–47 (1999).

28. S. Kodama and I. Kataoka, "Critical Heat Flux Prediction Method Based on Two-Phase Turbulence Model," *Journal of Nuclear Science and Technology*, 40(10), 725–733 (2003).

29. L. Vyskocil and J. Macek, "CFD Simulation of the Departure from Nucleate Boiling," *Proc. of the 16th International Topical Meeting on Nuclear Reactor Thermal Hydraulics* (*NURETH-16*), Chicago, IL, USA, August 30–September 4 (2015).

30. J. Pan, R. Li, D. Yang, and G. Wu, "Critical Heat Flux Prediction Model for Low Quality Flow Boiling of Water in Vertical Circular Tube," *International Journal of Heat and Mass Transfer*, 99, 243–251 (2016).

31. N. Yu and Y. Zhang, "Prediction of the Critical Heat Flux in Subcooled Flow Boiling in Round Tube Using an Improved Mechanistic Model," *Proc. of the 18th International Conference on Nuclear Engineering* (*ICONE18*), Xi'an, China, May 17–21 (2010).

32. S. Levy, "Forced Convection Subcooled Boiling – Prediction of Vapor Volumetric Fraction," *International Journal of Heat and Mass Transfer*, 10, 951–965 (1967).

33. S. W. Staub, "The Void Fraction in Subcooled Boiling – Prediction of the Initial Point of Net Vapor Generation," *Journal of Heat Transfer*, 90, 151–157 (1968).

34. H. Kinoshita, H. Nariai, and F. Inasaka, "Study of Critical Heat Flux Mechanism in Flow Boiling using Bubble Crowding Model," *JSME International Journal*, 44(1), 81–89 (2001).

35. T. Mazzocco, W. Ambrosini, R. Kommajosyula, and E. Baglietto, "A Reassessed Model for Mechanistic Prediction of Bubble Departure and Lift Off Diameters," *International Journal of Heat and Mass Transfer*, 117, 119–124 (2018).

36. N. E. Todreas and M. S. Kazimi, *Nuclear Systems, Volume 1: Thermal Hydraulic Fundamentals*, Second Edition, CRC Press, Taylor & Francis Group (2012).

37. P. Sara and N. Zuber, "Point of Net Vapor Generation and Vapor Void Fraction in Subcooled Boiling," *Proc. of the 5th International Heat Transfer Conference*, B4.7, Tokyo, Japan (1974).

38. U. Forssell and P. Lindskog, "Combining Semi-Physical and Neural Network Modeling: An Example of Its Usefulness," *International Federation of Automatic Control* (*IFAC*) *Symposium on System Identification*,767–770, Kitakyushu, Fukuoka, Japan (1997).